PROCEEDINGS A

royalsocietypublishing.org/journal/rspa

Research

Cite this article: Tang Y, Wang W, Duan H, Liu K. 2026 Concurrent topology and geometry optimization of origami structures via strain energy minimization. *Proc. R. Soc. A* **482**: 20260207.
https://doi.org/10.1098/rspa.2026.0207

Received: 14 March 2026
Accepted: 2 June 2026

Subject Areas:
mechanical engineering, structural engineering, mechanics

Keywords:
bar-and-hinge model, self-organization, topology optimization, geometry optimization, origami

Author for correspondence:
Ke Liu
e-mail: liuke@pku.edu.cn

†These authors contributed equally to this study.

Electronic supplementary material is available online at https://doi.org/10.6084/m9.figshare.c.8561980.

THE ROYAL SOCIETY PUBLISHING

Concurrent topology and geometry optimization of origami structures via strain energy minimization

Yansong Tang[1,†], Weiwei Wang[2,†], Huiling Duan[1] and Ke Liu[1]

[1]School of Advanced Manufacturing and Robotics, Peking University, Beijing 100871, People's Republic of China
[2]School of Mathematics, Statistics and Mechanics, Beijing University of Technology, Beijing 100124, People's Republic of China

HD, 0000-0003-1478-5649; KL, 0000-0001-9081-6334

Origami with programmable mechanical responses has emerged as an important topic in mechanics and materials research. Its geometric design space offers substantial tunability in stiffness, stability and deformation modes. However, the design of origami structures, especially non-rigid ones, remains a formidable challenge. Inspired by the self-organization of thin sheets into stable, low-energy origami configurations in nature, this paper proposes a unified optimization framework for rigid and non-rigid origami patterns via concurrent topology and geometry optimization. The framework uses the nonlinear bar-and-hinge model, which represents panel bending and crease folding within a unified hinge constitutive model. Consequently, topology optimization is achieved by switching between bending and folding hinges. Meanwhile, geometry optimization is achieved by adjusting the locations of origami vertices. Sensitivity analysis is carried out to enable the use of efficient gradient-based algorithms. Several numerical examples are provided, including the reproduction of origami bases, the Miura-ori and the Kresling tube, representing both rigid and non-rigid

origami patterns. These examples demonstrate the effectiveness and versatility of the proposed method, highlighting its potential for mechanically efficient and innovative origami design.

https://royalsocietypublishing.org/journal/rspa Proc. R. Soc. A 482: 20260207

1. Introduction

Origami, the ancient art of folding thin sheets along prescribed creases, has evolved into a rigorous framework for modern engineering design [1–3] (figure 1). Its folding-induced geometric design space offers exceptional tunability in stiffness, stability and deformation modes, enabling a wide range of mechanical functions [4–7]. As a result, origami-inspired structures have been increasingly explored across mechanics, physics and engineering, with demonstrated capabilities such as negative Poisson's ratio [8–10], multi-stability [11–13], high stiffness-to-weight ratios [14–16] and enhanced energy absorption [17–19]. These behaviours arise from the coupling among crease geometry, material response and boundary conditions, highlighting the need for design methodologies that are both geometrically expressive and mechanically informed.

A central challenge in origami design is to generate crease patterns that realize a desired three-dimensional configuration while simultaneously achieving favourable mechanical performance. Early computational tools, such as TreeMaker [1,20] and Origamizer [21,22], as well as classical tessellations, such as the Miura-ori [23–25], Resch [26–28] and Kresling [12,29,30] patterns, have enabled systematic geometric construction of foldable shapes. However, most of these methods are rooted in the rigid origami assumption, i.e. panels are treated as undeformable and deformation is confined to creases [31–33]. As a consequence, they are primarily suited for designing rigid origami and may lose accuracy when panel compliance, bending and material effects play an essential role.

In parallel with rapidly expanding applications in aerospace [34–37], metamaterials [3,38–41], medical devices [42–45] and robotics [46–48], the emphasis of origami design has gradually shifted from purely geometric feasibility towards mechanics-aware, performance-driven design. To this end, several mechanical models for non-rigid origami have been developed [49–54]. Among them, the nonlinear bar-and-hinge model [51] is attractive for computational design because it provides a unified description of panel bending and crease folding with relatively low computational cost [55]. Building upon such models, optimization-based approaches have shown promise in designing origami metamaterials [56–61] and compliant mechanisms [37,62–64]. Nevertheless, a unified framework that couples crease-pattern generation and mechanical deformation analysis for both rigid and non-rigid origami remains highly desirable.

Natural thin-sheet systems suggest a mechanics-driven design principle: creases emerge through self-organization under spatial constraints, and the resulting patterns are closely associated with energy minimization [65–70]. For example, Miura-like patterns can develop in compressed leaves [71–73], and Kresling-type patterns can arise in twisted cylindrical structures [12,74–77]. Related thin-sheet instabilities, such as wrinkling in multilayer soft substrate systems and functional properties engineered via buckling, have also attracted increasing attention [78,79]. In these systems, folds tend to appear in regions of large bending curvature, and their formation reduces the structural strain energy under the imposed constraints [65,67,71]. Similar mechanics-driven folding and buckling phenomena have been discussed in insect wings [80,81] and in cerebral cortical folding [82–84], as well as in mechanically induced protein unfolding [85–87]. This observation motivates a mechanics-driven design principle: crease patterns can be treated as designable 'soft' regions whose evolution is governed by strain-energy minimization.

In contrast to prior work, the present framework offers three main features. First, unlike geometric tools limited to rigid origami, it treats crease generation as strain-energy-driven mechanical evolution, enabling unified design of rigid and non-rigid origami. Second, instead of relying on a fixed topology or predetermined crease layout, it introduces a continuous crease indicator that allows the topology to emerge freely from an unstructured mesh. Third, it uniquely

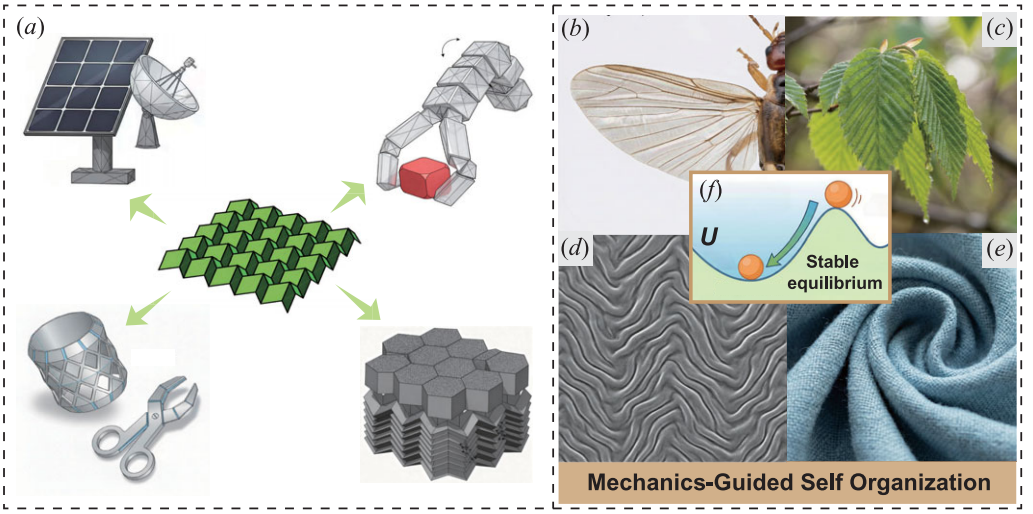

Figure 1. (*a*) Engineering applications of origami structures. (*b*) Close-up view of the earwig wing. (*c*) Leaf of the hornbeam. (*d*) Spontaneously formed quasi-Miura origami pattern of a buckled thin film on a soft substrate. (*e*) Quasi-axially expanded radial origami configuration of the buckled twisted fabric. (*f*) Schematic illustration of the principle of minimum potential energy.

couples topology and geometry optimization, simultaneously identifying crease locations and refining nodal positions within a unified energy-minimization framework.

Motivated by this principle, this paper proposes a unified optimization design framework for both rigid and non-rigid origami patterns based on concurrent topology and geometry optimization. The framework employs the nonlinear bar-and-hinge model for simulation, in which panel bending and crease folding are represented within a unified hinge constitutive model. Accordingly, topology optimization is performed by switching hinges between bending- and folding-dominated behaviour via continuous design variables, while geometry optimization is performed by adjusting the locations of origami vertices. Sensitivity analyses are derived to enable efficient gradient-based optimization. Several numerical examples are provided, including the reproduction of basic origami bases, the Miura-ori and the Kresling tube.

The remainder of this paper is organized as follows. Section 2 presents the problem formulation and preliminaries. Section 3 presents the formulation and sensitivity analysis, §4 summarizes the optimization algorithms, §5 provides numerical examples, and §6 concludes the paper.

2. Problem formulation and preliminaries

This section introduces the mechanical and optimization preliminaries required by the proposed framework. It briefly reviews the nonlinear bar-and-hinge model used to simulate coupled panel bending and crease folding, and then defines the continuous crease indicator together with the associated interpolation functions that characterize the design space.

(a) Bar-and-hinge model for mechanical analysis

The bar-and-hinge model [51,88] provides distinct advantages for the analysis of thin-walled origami structures, particularly in terms of computational efficiency and a straightforward methodology for crease definition. As illustrated in figure 2, this discretized model utilizes bar elements to capture in-plane tensile and compressive behaviour, while torsional springs represent out-of-plane bending and folding deformations of the panels. Within this kinematic

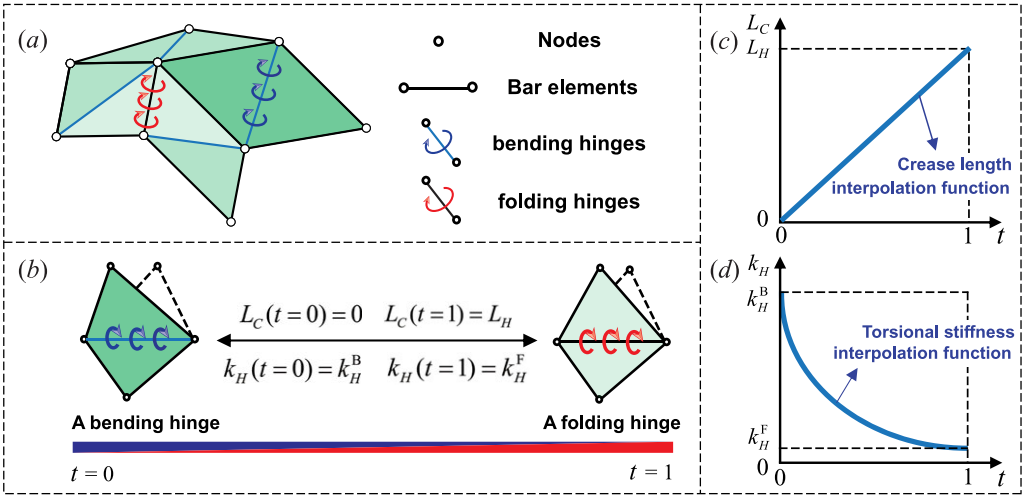

Figure 2. (*a*) Schematic of the bar-and-hinge discretization. (*b*) Physical properties at the upper and lower limits of the crease indicator. (*c*) Interpolation function relating the design variable t to the equivalent crease length. (*d*) Interpolation function relating t to the torsional stiffness of the hinge.

framework, Liu and Paulino formulated a displacement-based, fully nonlinear quasi-static governing equation for the mechanical analysis of origami structures, which has been shown to effectively capture both buckling and post-buckling responses [57].

In non-rigid origami, deformation localizes primarily at the creases, where the bending stiffness is significantly lower than that of the panels. Accordingly, folding behaviour is modelled using folding hinges along the creases, while panel bending is represented by bending hinges, as shown in figure 2a. Typically, the torsional stiffness of a folding hinge (k_H^{F}) is significantly lower than that of a bending hinge (k_H^{B}), as illustrated in figure 2b. By employing the same constitutive relationship for both types of hinges but with different stiffness values, a seamless transition between the two states is achieved, which is essential for the subsequent topology optimization.

(b) Crease indicator and interpolation functions for physical properties

Inspired by continuum topology optimization, we introduce a continuous design variable $t \in [0,1]$ to indicate the state of a hinge element. As shown in figure 2b, a value of $t=1$ corresponds to a folding hinge, which essentially acts as a crease, whereas $t=0$ represents a bending hinge that models a panel. Intermediate values $0<t<1$ describe a transitional state between these two extremes. The mapping between the physical properties and the design variable t is illustrated in figure 2c,d. The equivalent crease length L_C and the torsional stiffness k_H of a hinge element are defined through the following interpolation functions:

$$L_{Cj}(t_j) = f_L(t_j) L_{Hj}^0 \quad \text{and} \quad f_L(t_j) = t_j \tag{2.1}$$

and

$$k_{Hj}(t_j) = f_k(t_j) k_H^{\mathrm{B}}, \quad f_k(t_j) = 1 - \beta t_j^3 \quad \text{and} \quad \beta = 1 - \frac{k_H^{\mathrm{F}}}{k_H^{\mathrm{B}}}, \tag{2.2}$$

where L_{Hj}^0 is the initial length of hinge j, and $k_{Hj}(t_j)$ is its torsional stiffness as a function of the topology variable t_j. The subscript j will be used throughout to indicate quantities pertaining to hinge j. k_H^{B} and k_H^{F} denote the torsional stiffnesses of the bending and folding hinges, respectively, with $k_H^{\mathrm{B}} \gg k_H^{\mathrm{F}}$; $f_L(t)$ and $f_k(t)$ are the interpolation functions for crease length and torsional stiffness; and β is a constant coefficient that depends on the relative stiffness of the two hinge types. This

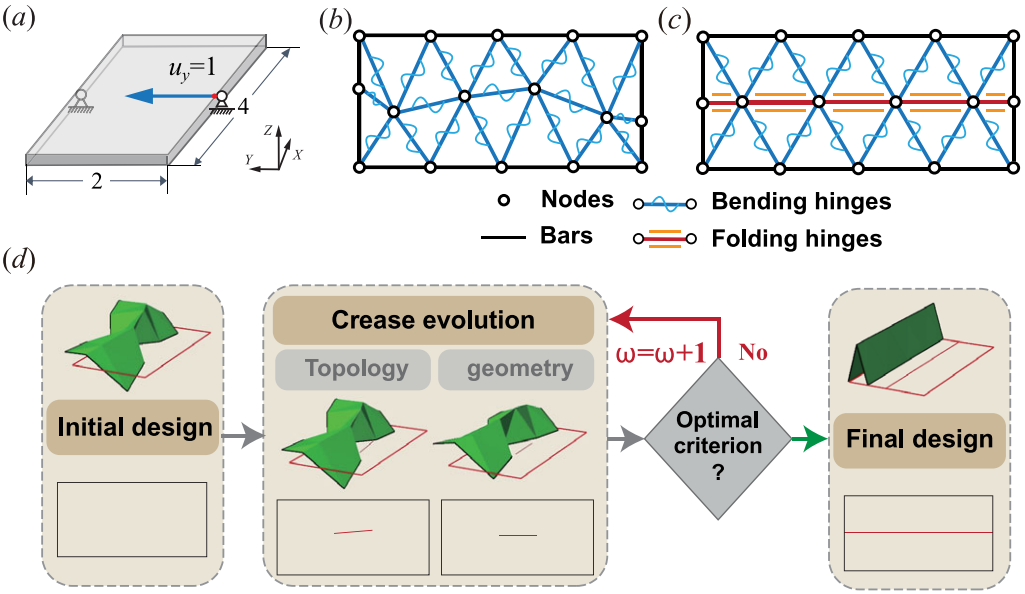

Figure 3. Concept of crease evolution illustrated through a centre-folding problem. (*a*) Geometric parameters and boundary conditions. (*b*) Initial bar-and-hinge discretization. (*c*) Final bar-and-hinge model with evolved crease pattern. (*d*) Sequential evolution of the crease topology and nodal positions.

interpolation scheme smoothly connects the two extreme states and enables a continuous design space for optimization.

The bar-and-hinge discretization and the crease-indicator interpolation establish a continuous, mechanics-consistent design space. Section 3 presents the unified optimization formulation and the associated solution procedure.

3. Optimization formulation and sensitivity analysis

This section presents the unified formulation for the concurrent topology and geometry optimization of origami structures and derives the corresponding sensitivity expressions under displacement-controlled loading. The explicit approximations for the topology and geometry subproblems are also introduced to facilitate the subsequent update of the design variables.

(a) Unified optimization formulation

(i) Optimization problem statement

We formulate a unified optimization problem to capture the coupled evolution of crease topology and vertex geometry under displacement-controlled loading. We illustrate the formulation using a straight-fold example (figure 3a). The structure is modelled by the nonlinear bar-and-hinge representation with both bending and folding springs (figure 3b,c). Topology and geometry optimization are then combined to minimize the equilibrium strain energy and to emulate progressive crease emergence (figure 3d). Starting from an initial random mesh (figure 3b), the iterative updates yield an evolved crease pattern and its associated deformation mode (figure 3c).

The objective of this unified optimization is to minimize the structural strain energy U when the structure is in equilibrium under prescribed spatial constraints $\boldsymbol{u}_d$. This requires the simultaneous evolution of two types of design variables: the topological design variables $\boldsymbol{t}$ that indicate the existence and strength of creases, and the nodal coordinates $\boldsymbol{x}$ that define the

geometry. The optimization problem for the $(\omega+1)$th evolution step is formulated as

$$\begin{cases} \min_{t,x} & U(\boldsymbol{t},\boldsymbol{x}), \\ \text{s.t.} & \sum_{j=1}^{N_2} L_{Hj}^0 t_j \le \overline{C}_{\text{dy}}^{(\omega+1)} \cdot \sum_{j=1}^{N_2} L_{Hj}^0, \\ & \dfrac{\partial \Pi}{\partial \boldsymbol{u}} = \boldsymbol{0}, \\ & \boldsymbol{D}\boldsymbol{u} = \boldsymbol{u}_d, \\ & t_{\min} \le t_j \le 1, \quad j = 1,\ldots,N_2, \\ & \underline{x}_m^{(\omega+1)} \le x_m \le \overline{x}_m^{(\omega+1)}, \quad m = 1,\ldots,M. \end{cases} \tag{3.1}$$

The objective is to minimize the total strain energy $U(\boldsymbol{t},\boldsymbol{x})$ of the structure. The first constraint limits the total equivalent crease length to a prescribed fraction of the total hinge length, where $\overline{C}_{\text{dy}}$ is an adaptive crease_length ratio that increases monotonically with the evolution step ω to allow progressive crease emergence. We adopt a linear schedule for $\overline{C}_{\text{dy}}^{(\omega)}$ gradually increasing it from a small initial value to a prescribed maximum over the major iterations to ensure a smooth emergence of crease patterns. The second constraint enforces mechanical equilibrium, where Π is the total potential energy of the structure and $\boldsymbol{u}$ is the nodal displacement vector. The third constraint prescribes the displacements on certain degrees of freedom, with $\boldsymbol{D}$ being a Boolean selection matrix that extracts the prescribed displacements $\boldsymbol{u}_d$. The fourth constraint for all hinges $j = 1,\ldots,N_2$ imposes simple bounds on the topology variables, where $t_{\min}$ is a small positive lower bound introduced to avoid numerical singularity. Finally, the fifth constraint for all optimized coordinate components $m = 1,\ldots,M$ defines move limits on the nodal coordinates, where $\underline{x}_m$ and $\overline{x}_m$ are the lower and upper bounds for the nodal coordinates, and M is the number of nodal coordinate components to be optimized.

The structural strain energy in the bar-and-hinge model is given by

$$U = \sum_{i=1}^{N_1} U_{Bi} + \sum_{j=1}^{N_2} U_{Hj}, \tag{3.2}$$

where U_{Bi} and U_{Hj} denote the strain energies of bar element i and hinge element j, respectively, and N_1 and N_2 are the total numbers of bar and hinge elements.

The decision to terminate the crease evolution may depend on various user-defined criteria. A common stopping criterion based on the relative reduction in strain energy is

$$\left| \frac{U^{(\omega+1)*} - U^{(\omega)*}}{U^{(\omega)*}} \right| \le \phi, \tag{3.3}$$

where $U^{(\omega)*}$ is the optimal strain energy at step ω, and ϕ is a prescribed threshold.

(ii) Sensitivity analysis under displacement-controlled loading

To efficiently solve the coupled topology and geometry optimization problem, gradient information is required to guide the update of design variables. We derive the sensitivity of the structural strain energy with respect to an arbitrary design parameter α. Here, α represents a generic design variable that can be either a topology variable t_j or a nodal coordinate x_m.

When the structure is in equilibrium, the principle of minimum potential energy holds:

$$\frac{\delta \Pi}{\delta \boldsymbol{u}} = \frac{\delta (U - V)}{\delta \boldsymbol{u}} = \frac{\delta U}{\delta \boldsymbol{u}} - \frac{\delta V}{\delta \boldsymbol{u}} = \boldsymbol{T}(\boldsymbol{u},\alpha) - \boldsymbol{F}(\boldsymbol{u},\alpha) = \boldsymbol{0}, \tag{3.4}$$

where V is the work done by external forces, and $\boldsymbol{T}$ and $\boldsymbol{F}$ denote the nodal internal and external force vectors, respectively.

Under displacement control, the displacement and force vectors can be partitioned into free (f) and prescribed (d) degrees of freedom. The external forces at the free degrees of freedom vanish

https://royalsocietypublishing.org/journal/rspa Proc. R. Soc. A 482: 20260207

($\boldsymbol{F}_f = \boldsymbol{0}$), and the prescribed displacements $\boldsymbol{u}_d$ are independent of the design variable α, which leads directly to the orthogonality condition

$$\boldsymbol{F}^{\mathsf{T}} \frac{\mathrm{d}\boldsymbol{u}}{\mathrm{d}\alpha} = \boldsymbol{0}. \tag{3.5}$$

Combining equations (3.4) and (3.5), the total derivative of the strain energy with respect to α is derived as

$$\begin{aligned} \frac{\mathrm{d}U(\boldsymbol{u},\alpha)}{\mathrm{d}\alpha} &= \frac{\partial U(\boldsymbol{u},\alpha)}{\partial \alpha} + \frac{\partial U(\boldsymbol{u},\alpha)}{\partial \boldsymbol{u}} \frac{\mathrm{d}\boldsymbol{u}}{\mathrm{d}\alpha} \\ &= \frac{\partial U(\boldsymbol{u},\alpha)}{\partial \alpha} + \boldsymbol{F}^{\mathsf{T}} \frac{\mathrm{d}\boldsymbol{u}}{\mathrm{d}\alpha} \qquad (3.6) \\ &= \frac{\partial U(\boldsymbol{u},\alpha)}{\partial \alpha}. \qquad (3.7) \end{aligned}$$

Equation (3.7) indicates that, under displacement-controlled loading, the total derivative of the strain energy with respect to a design parameter reduces to its partial derivative with the displacement field held fixed. This simplification avoids the computationally expensive calculation of the displacement derivatives. It is important to note that this conclusion holds only for displacement-controlled loading. In the case of force-controlled loading, the orthogonality condition would not hold and the displacement derivative term would need to be included. All optimization problems studied in this work are displacement-controlled, hence the simplified expression (equation (3.7)) is applicable throughout.

Since the total strain energy is the sum of contributions from bars and hinges (equation (3.2)), the sensitivity can be expressed as

$$\frac{\mathrm{d}U}{\mathrm{d}\alpha} = \sum_{i=1}^{N_1} \frac{\partial U_{Bi}}{\partial \alpha} + \sum_{j=1}^{N_2} \frac{\partial U_{Hj}}{\partial \alpha}. \tag{3.8}$$

Equation (3.8) provides the foundation for computing specific sensitivities with respect to the topology variables t_j and nodal coordinates x_m. In the subsequent subsections, explicit expressions for $\partial U_{Bi}/\partial t_j$, $\partial U_{Hj}/\partial t_j$, $\partial U_{Bi}/\partial x_m$ and $\partial U_{Hj}/\partial x_m$ will be derived, enabling the efficient update of design variables in the optimization algorithm.

(b) Origami topology optimization

(i) Topology optimization formulation

In the topology optimization stage, the background grid is kept fixed and the crease pattern is determined by optimizing the hinge indicators $\boldsymbol{t}$. The corresponding optimization problem is

$$\begin{cases} \min_{\boldsymbol{t}} & U(\boldsymbol{t}) = \sum_{i=1}^{N_1} U_{Bi} + \sum_{j=1}^{N_2} U_{Hj}(\boldsymbol{t}); \\ \text{s.t.} & \sum_{j=1}^{N_2} L_{Hj}^0 t_j \le \overline{C}_{\mathrm{dy}} \cdot \sum_{j=1}^{N_2} L_{Hj}^0; \\ & \dfrac{\partial \Pi}{\partial \boldsymbol{u}} = \boldsymbol{0}; \\ & t_{\min} \le t_j \le 1 \quad (j = 1, \ldots, N_2). \end{cases} \tag{3.9}$$

Here, the objective is to minimize the total strain energy $U(\boldsymbol{t})$ with respect to the topology design variables $\boldsymbol{t} = [t_1, \ldots, t_{N_2}]^{\mathsf{T}}$. The first constraint limits the total equivalent crease length, where $\overline{C}_{\mathrm{dy}}$ is the dynamic crease-length ratio. The second constraint enforces mechanical equilibrium. The variables t_j are bounded between a small positive lower bound $t_{\min}$ and 1.

The problem is solved iteratively. At each iteration, the design variables are updated based on the mechanical response, the sensitivity information and an explicit approximation of the objective, as described below.

(ii) Sensitivity analysis with respect to topology variables

From the strain-energy expression (equation (3.2)) and the interpolation functions (equations (2.1) and (2.2)), the topology variables t_j affect the objective only through the hinge torsional stiffness and, consequently, the hinge strain energy U_{Hj}. The strain energies of bar element i and hinge element j are

$$U_{Bi} = W_i L_{Bi} A \tag{3.10}$$

and

$$U_{Hj} = \frac{1}{2} k_{Hj} L^0_{Hj} (\theta'_j - \theta_j)^2, \tag{3.11}$$

where W_i is the strain-energy density of bar i; A is the cross-sectional area of a bar element; L_{Bi} and L^0_{Hj} are the initial lengths of bar i and hinge j, respectively; k_{Hj} is the torsional stiffness of hinge j; and θ_j and θ'_j are the dihedral angles before and after deformation.

The sensitivity of the hinge strain energy with respect to t_j follows from the chain rule. From equation (3.11),

$$\frac{\partial U_{Hj}}{\partial t_j} = \frac{1}{2} \frac{\partial k_{Hj}}{\partial t_j} L^0_{Hj} (\theta'_j - \theta_j)^2 + k_{Hj} L^0_{Hj} (\theta'_j - \theta_j) \frac{\partial (\theta'_j - \theta_j)}{\partial t_j}.$$

Under displacement-controlled loading, the displacement field is held fixed when taking partial derivatives. Hence, $\theta'_j - \theta_j$ is independent of t_j, the second term vanishes and we obtain

$$\frac{\partial U_{Hj}}{\partial t_j} = \frac{1}{2} \frac{\partial k_{Hj}}{\partial t_j} L^0_{Hj} (\theta'_j - \theta_j)^2 = \frac{U_{Hj}}{k_{Hj}} \cdot \frac{\partial k_{Hj}}{\partial t_j}.$$

Using the stiffness interpolation (equation (2.2)), the sensitivity becomes

$$\frac{\partial U_{Hj}}{\partial t_j} = \frac{-3\beta t_j^2}{1 - \beta t_j^3} U_{Hj}(t_j). \tag{3.12}$$

These sensitivity expressions are then used to construct an explicit approximation of the objective function and to update the design variables.

(iii) Explicit approximation and linearized subproblem

To obtain an efficient update scheme, we construct an explicit approximation of the objective function. Since U_{Bi} does not depend explicitly on t_j and under displacement-controlled loading $\mathrm{d}U/\mathrm{d}t_j = \partial U/\partial t_j$ (equation (3.7)), it suffices to linearize only the hinge energy contribution. Using a first-order Taylor expansion about the current design $\boldsymbol{t}^{(v)}$, where v denotes the iteration number within the topology optimization, the total strain energy is approximated as

$$U(\boldsymbol{t}) \approx U^{(v)} + \sum_{j=1}^{N_2} \left. \frac{\partial U_{Hj}}{\partial t_j} \right|_{\boldsymbol{t}=\boldsymbol{t}^{(v)}} (t_j - t_j^{(v)}), \tag{3.13}$$

with $U^{(v)} = \sum_i U_{Bi}^{(v)} + \sum_j U_{Hj}^{(v)}$.

Substituting equation (3.12) into equation (3.13) yields the explicit approximation:

$$U(\boldsymbol{t}) \approx U^{(v)} + \sum_{j=1}^{N_2} a_j^{(v)} (t_j - t_j^{(v)}) \quad \text{with } a_j^{(v)} = \frac{-3\beta (t_j^{(v)})^2}{1 - \beta (t_j^{(v)})^3} U_{Hj}^{(v)}. \tag{3.14}$$

Since the constant term $U^{(v)} - \sum_j a_j^{(v)} t_j^{(v)}$ does not affect the optimum, minimizing $U(\boldsymbol{t})$ is equivalent to minimizing the linearized objective

$$\widetilde{U}(\boldsymbol{t}) = \sum_{j=1}^{N_2} a_j^{(v)} t_j. \tag{3.15}$$

Because $\beta > 0$, the coefficients $a_j^{(v)}$ are negative. Hence, minimizing $\widetilde{U}(\boldsymbol{t})$ is equivalent to maximizing the weighted sum $\sum_{j=1}^{N_2} |a_j^{(v)}| t_j$. Under the crease-length constraint, this implies that larger t_j values are preferentially assigned to hinges with larger absolute sensitivity $|a_j^{(v)}|$, i.e. hinges that most effectively reduce the objective.

Similarly, the crease-length constraint in equation (3.9) can be rewritten using the length interpolation (equation (2.1)) as

$$\sum_{j=1}^{N_2} L_{Hj}^0 t_j \le \overline{C}_{\mathrm{dy}} \cdot \sum_{j=1}^{N_2} L_{Hj}^0. \tag{3.16}$$

Consequently, at each iteration v, the above linearization yields the following linearized subproblem:

$$\begin{cases} \min_{\boldsymbol{t}} & \widetilde{U}(\boldsymbol{t}) = \sum_{j=1}^{N_2} a_j^{(v)} t_j, \\ \text{s.t.} & \sum_{j=1}^{N_2} L_{Hj}^0 t_j \le \overline{C}_{\mathrm{dy}} \cdot \sum_{j=1}^{N_2} L_{Hj}^0, \\ & t_{\min} \le t_j \le 1 \quad (j = 1, \ldots, N_2). \end{cases} \tag{3.17}$$

In this work, this linearized subproblem is handled using an optimality criteria (OC) update with a Lagrange multiplier to enforce the crease-length constraint and the bound constraints, which is summarized in §4a.

(c) Origami geometry optimization

(i) Geometry optimization formulation

To refine crease geometry and mitigate mesh dependency, we formulate a geometry optimization problem in which the nodal coordinates are treated as design variables. Let the total number of nodes be N. We collect all nodal coordinates in the vector $\boldsymbol{x} = [x_1, y_1, z_1, x_2, y_2, z_2, \ldots, x_N, y_N, z_N]^{\mathrm{T}}$. The total number of design variables is denoted by M; in the special case where all nodal coordinates are optimized, $M = 3N$. The goal is to minimize the structural strain energy under prescribed displacement constraints. The geometry optimization problem at a given evolution step is

$$\begin{cases} \min_{x} & U(\boldsymbol{x}), \\ \text{s.t.} & \underline{x}_m \le x_m \le \overline{x}_m, \quad m = 1, \ldots, M, \end{cases} \tag{3.18}$$

where $\boldsymbol{x} = [x_1, \ldots, x_M]^{\mathrm{T}}$ denotes the vector of nodal coordinates to be optimized. Thus, each x_m is a scalar representing one coordinate component of a specific node. The bounds $\underline{x}_m$ and $\overline{x}_m$ define a trust region around the current design to ensure smooth geometric evolution. These bounds are updated at each evolution step ω as

$$\underline{x}_m = x_m^{(\omega)*} - \Delta s \quad \text{and} \quad \overline{x}_m = x_m^{(\omega)*} + \Delta s, \tag{3.19}$$

where $x_m^{(\omega)*}$ is the optimal coordinate from the previous evolution step. The move limit Δs is chosen as

$$\Delta s = \eta \cdot \min(\boldsymbol{L}), \tag{3.20}$$

with $\eta \in (0, 1]$ being a scaling factor and $\min(\boldsymbol{L})$ the minimum initial bar length in the structure. The actual step size used in each geometry iteration is obtained by dividing Δs by the number of inner iterations N_S, i.e., $move = \Delta s / N_S$, as described in Section 4(b). This choice keeps geometry updates within a physically reasonable range.

(ii) Sensitivity analysis with respect to nodal coordinates

To solve the geometry optimization problem (equation (3.18)) efficiently, the sensitivity of the structural strain energy with respect to each design variable must be evaluated. Recall that each

design variable x_m corresponds to a specific coordinate component of a node. To facilitate the derivation, we introduce explicit notation for nodal coordinates and displacements. For a generic node p, we denote its position vector by $\boldsymbol{X}_p = [X_p, Y_p, Z_p]^\intercal$ and its displacement vector by $\boldsymbol{u}_p = [u_p^x, u_p^y, u_p^z]^\intercal$. When the design variable of interest is the x-coordinate of node p, we have $x_m = X_p$ for the corresponding index m; sensitivities with respect to Y_p or Z_p follow analogously. In the following, we present the derivation for X_p to illustrate the procedure.

We first note that the analysis is performed under displacement-controlled loading. From §3a(ii) (equation (3.7)), we have $\mathrm{d}U/\mathrm{d}X_p = \partial U/\partial X_p$; that is, the contribution from the derivative of the displacement field vanishes. Hence, when computing $\partial U/\partial X_p$, the displacement field can be held fixed, and all displacement components u_p^x, u_p^y, u_p^z are treated as constants.

The initial length of a bar element i connecting nodes p and q is

$$L_{Bi} = \sqrt{(X_p - X_q)^2 + (Y_p - Y_q)^2 + (Z_p - Z_q)^2}, \tag{3.21}$$

and its element displacement vector is $\boldsymbol{u}_i^{(e)} = [u_p^x, u_p^y, u_p^z, u_q^x, u_q^y, u_q^z]^\intercal$.

The strain energy of bar i is $U_{Bi} = W_i L_{Bi} A$, where W_i is the strain-energy density and A is the cross-sectional area. Applying the chain rule yields

$$\frac{\partial U_{Bi}}{\partial X_p} = W_i \frac{\partial L_{Bi}}{\partial X_p} A + \frac{\partial W_i}{\partial \mathcal{E}_i} \frac{d\mathcal{E}_i}{dX_p} L_{Bi} A, \tag{3.22}$$

with $\partial W_i/\partial \mathcal{E}_i = S_i$ being the axial stress in the bar.

For the bar elements in this study, we adopt a hyperelastic material model. The strain-energy density function takes the following form:

$$W_i = \frac{C}{\alpha_1 - \alpha_2} \left[\frac{(1 + 2\mathcal{E}_i)^{\alpha_1/2} - 1}{\alpha_1} - \frac{(1 + 2\mathcal{E}_i)^{\alpha_2/2} - 1}{\alpha_2} \right], \tag{3.23}$$

where C is the tangential elastic modulus, and α_1, α_2 are material constants. The Green-Lagrange strain for a bar element is expressed as

$$\mathcal{E}_i = \boldsymbol{B}_{Li} \boldsymbol{u}_i^{(e)} + \frac{1}{2} (\boldsymbol{u}_i^{(e)})^\intercal \boldsymbol{B}_{NLi} \boldsymbol{u}_i^{(e)}, \tag{3.24}$$

with $\boldsymbol{u}_i^{(e)} = [u_p^x, u_p^y, u_p^z, u_q^x, u_q^y, u_q^z]^\intercal$ being the element displacement vector. The linear and nonlinear strain-displacement matrices are defined as

$$\boldsymbol{B}_{Li} = \frac{[X_p - X_q, Y_p - Y_q, Z_p - Z_q, X_q - X_p, Y_q - Y_p, Z_q - Z_p]}{(L_{Bi})^2} \tag{3.25}$$

and

$$\boldsymbol{B}_{NLi} = \frac{1}{(L_{Bi})^2} \begin{bmatrix} \boldsymbol{I}_{3\times3} & -\boldsymbol{I}_{3\times3} \\ -\boldsymbol{I}_{3\times3} & \boldsymbol{I}_{3\times3} \end{bmatrix}, \tag{3.26}$$

where $\boldsymbol{I}_{3\times3}$ is the 3×3 identity matrix.

Now consider the sensitivity with respect to the x-coordinate of node p, denoted by X_p. The derivative of the strain can be decomposed into two parts: one through the change in bar length L_{Bi}, and one through the explicit dependence of the strain-displacement matrices on X_p:

$$\frac{\mathrm{d}\mathcal{E}_i}{\mathrm{d}X_p} = \frac{\partial \mathcal{E}_i}{\partial L_{Bi}} \frac{\partial L_{Bi}}{\partial X_p} + \frac{\partial \mathcal{E}_i}{\partial X_p}, \tag{3.27}$$

where the first term captures the dependence through L_{Bi}, and the second term captures the explicit dependence with L_{Bi} held constant.

https://royalsocietypublishing.org/journal/rspa Proc. R. Soc. A 482: 20260207

From the definitions of $\boldsymbol{B}_{Li}$ and $\boldsymbol{B}_{NLi}$, which are proportional to $1/L_{Bi}^2$, we have

$$\frac{\partial \boldsymbol{B}_{Li}}{\partial L_{Bi}} = -\frac{2}{L_{Bi}}\boldsymbol{B}_{Li} \quad \text{and} \quad \frac{\partial \boldsymbol{B}_{NLi}}{\partial L_{Bi}} = -\frac{2}{L_{Bi}}\boldsymbol{B}_{NLi}. \tag{3.28}$$

Applying the chain rule to $\mathcal{E}_i = \boldsymbol{B}_{Li}\boldsymbol{u}_i^{(e)} + \frac{1}{2}(\boldsymbol{u}_i^{(e)})^{\mathsf{T}}\boldsymbol{B}_{NLi}\boldsymbol{u}_i^{(e)}$ and using the above relations yields

$$\frac{\partial \mathcal{E}_i}{\partial L_{Bi}} = -\frac{2}{L_{Bi}}\left(\boldsymbol{B}_{Li}\boldsymbol{u}_i^{(e)} + \frac{1}{2}(\boldsymbol{u}_i^{(e)})^{\mathsf{T}}\boldsymbol{B}_{NLi}\boldsymbol{u}_i^{(e)}\right) = -\frac{2}{L_{Bi}}\mathcal{E}_i. \tag{3.29}$$

For the explicit derivative with a constant bar length, we consider L_{Bi} fixed and differentiate $\boldsymbol{B}_{Li}$ and $\boldsymbol{B}_{NLi}$ directly with respect to X_p. From equation (3.25):

$$\frac{\partial \boldsymbol{B}_{Li}}{\partial X_p} = \frac{1}{L_{Bi}^2}[1, 0, 0, -1, 0, 0],$$

and from equation (3.26), $\partial \boldsymbol{B}_{NLi}/\partial X_p = \boldsymbol{0}$ since $\boldsymbol{B}_{NLi}$ has no explicit dependence on individual coordinates.

$$\frac{\partial \mathcal{E}_i}{\partial X_p} = \frac{\partial \boldsymbol{B}_{Li}}{\partial X_p}\boldsymbol{u}_i^{(e)} = \frac{1}{L_{Bi}^2}(u_p^x - u_q^x). \tag{3.30}$$

The derivative of the bar length with respect to X_p follows from equation (3.21):

$$\frac{\partial L_{Bi}}{\partial X_p} = \frac{X_p - X_q}{L_{Bi}}. \tag{3.31}$$

Substituting equations (3.29), (3.31) and (3.30) into equation (3.27) yields the complete strain derivative:

$$\frac{\mathrm{d}\mathcal{E}_i}{\mathrm{d}X_p} = -\frac{2\mathcal{E}_i}{L_{Bi}} \cdot \frac{X_p - X_q}{L_{Bi}} + \frac{u_p^x - u_q^x}{L_{Bi}^2}. \tag{3.32}$$

The stress $S_i = \partial W_i/\partial \mathcal{E}_i$ for the hyperelastic model in equation (3.23) is obtained by differentiation:

$$S_i = \frac{\partial W_i}{\partial \mathcal{E}_i} = \frac{C}{\alpha_1 - \alpha_2}[(1 + 2\mathcal{E}_i)^{\alpha_1/2-1} - (1 + 2\mathcal{E}_i)^{\alpha_2/2-1}]. \tag{3.33}$$

For the final bar sensitivity, substituting equations (3.31), (3.32) and (3.33) into equation (3.22) yields the sensitivity of the bar strain energy with respect to X_p. For a bar connecting nodes p and q, we denote this sensitivity by H_{ip}, i.e.

$$\begin{aligned} H_{ip} &:= \frac{\partial U_{Bi}}{\partial X_p} \\ &= W_i \frac{X_p - X_q}{L_{Bi}} A + S_i L_{Bi} A \left(-\frac{2\mathcal{E}_i}{L_{Bi}} \cdot \frac{X_p - X_q}{L_{Bi}} + \frac{u_p^x - u_q^x}{L_{Bi}^2}\right) \\ &= \frac{X_p - X_q}{L_{Bi}^2} U_{Bi} + S_i A \left(-2\mathcal{E}_i \frac{X_p - X_q}{L_{Bi}} + \frac{u_p^x - u_q^x}{L_{Bi}}\right), \end{aligned} \tag{3.34}$$

where H_{ip} represents the contribution of bar i to the sensitivity with respect to the x-coordinate of node p.

For the sensitivity contribution from a hinge element j, its strain energy is given by $U_{Hj} = \frac{1}{2}k_{Hj}L_{Hj}(\theta_j' - \theta_j)^2$, which depends on the hinge length L_{Hj} and the undeformed and deformed dihedral angles θ_j and θ_j'. In the geometry optimization stage, L_{Hj} is defined as the distance between the two nodes that form the hinge line in the current reference configuration; hence L_{Hj} varies with the nodal coordinates. This is distinct from the fixed initial hinge length L_{Hj}^0 used in topology optimization. As illustrated in figure 4, a hinge j typically involves four nodes: a and d on the hinge line, and b and c off the line that define the adjacent facets. We denote their position vectors by $\boldsymbol{X}_a, \boldsymbol{X}_b, \boldsymbol{X}_c, \boldsymbol{X}_d$, with $\boldsymbol{X}_\cdot = [X_\cdot, Y_\cdot, Z_\cdot]^{\mathsf{T}}$, and displacement vectors by $\boldsymbol{u}_\cdot = [u_\cdot^x, u_\cdot^y, u_\cdot^z]^{\mathsf{T}}$. To

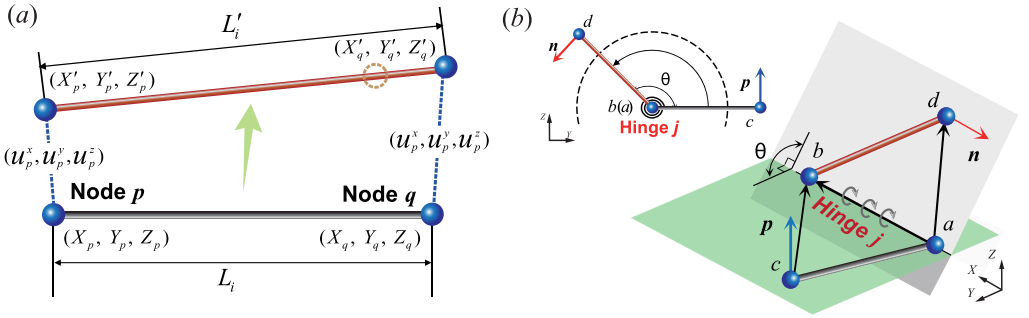

Figure 4. (*a*) Schematic of a single bar element before and after deformation. (*b*) Three-dimensional vector diagram of hinge *j* and side view of the vectors.

obtain the sensitivity with respect to a specific nodal coordinate, say the x-coordinate X_a of node a, we apply the chain rule:

$$\frac{\partial U_{Hj}}{\partial X_a} = \frac{k_{Hj}}{2}\frac{\partial L_{Hj}}{\partial X_a}(\theta_j' - \theta_j)^2 + k_{Hj}L_{Hj}(\theta_j' - \theta_j)\left(\frac{\partial \theta_j'}{\partial X_a} - \frac{\partial \theta_j}{\partial X_a}\right), \tag{3.35}$$

where θ_j and θ_j' are the dihedral angles before and after deformation. Under displacement-controlled loading, the deformed x-coordinate of node a is $X_a' = X_a + u_a^x$, and since the displacement u_a^x is prescribed and held fixed when taking partial derivatives, we have $\partial X_a'/\partial X_a = 1$; consequently $\partial \theta_j'/\partial X_a = \partial \theta_j'/\partial X_a'$.

The derivative $\partial L_{Hj}/\partial X_a$ is computed analogously to the bar element case. For a hinge whose line connects nodes a and d (figure 4), if we consider the x-coordinate of node a, denoted by X_a, then

$$\frac{\partial L_{Hj}}{\partial X_a} = \frac{X_a - X_d}{L_{Hj}}. \tag{3.36}$$

The derivative of the dihedral angle, $\partial \theta_j/\partial X_a$, depends on the specific nodal arrangement within the hinge and has been established in the literature [51]. For a hinge defined by four nodes a, b, c, d (figure 4), with coordinate vectors $\boldsymbol{X}_a, \boldsymbol{X}_b, \boldsymbol{X}_c, \boldsymbol{X}_d$, we define the vectors:

$$\boldsymbol{r}_{ba} = \boldsymbol{X}_a - \boldsymbol{X}_b, \quad \boldsymbol{r}_{bc} = \boldsymbol{X}_c - \boldsymbol{X}_b \quad \text{and} \quad \boldsymbol{r}_{da} = \boldsymbol{X}_a - \boldsymbol{X}_d \tag{3.37}$$

and

$$\boldsymbol{n} = \boldsymbol{r}_{ba} \times \boldsymbol{r}_{da} \quad \text{and} \quad \boldsymbol{p} = \boldsymbol{r}_{ba} \times \boldsymbol{r}_{bc}. \tag{3.38}$$

The dihedral angle θ_j (see figure 4) satisfies

$$\cos\theta_j = \frac{(\boldsymbol{r}_{ba} \times \boldsymbol{r}_{da}) \cdot (\boldsymbol{r}_{ba} \times \boldsymbol{r}_{bc})}{||\boldsymbol{r}_{ba} \times \boldsymbol{r}_{da}||\,||\boldsymbol{r}_{ba} \times \boldsymbol{r}_{bc}||}.$$

Differentiating this expression with respect to the nodal coordinates using vector calculus identities yields the following derivatives [51]:

$$\frac{\partial \theta_j}{\partial \boldsymbol{X}_d} = \frac{||\boldsymbol{r}_{ba}||}{||\boldsymbol{n}||^2}\boldsymbol{n}, \quad \frac{\partial \theta_j}{\partial \boldsymbol{X}_c} = -\frac{||\boldsymbol{r}_{ba}||}{||\boldsymbol{p}||^2}\boldsymbol{p}, \tag{3.39}$$

$$\frac{\partial \theta_j}{\partial \boldsymbol{X}_a} = \left(\frac{\boldsymbol{r}_{da} \cdot \boldsymbol{r}_{ba}}{||\boldsymbol{r}_{ba}||^2} - 1\right)\frac{\partial \theta_j}{\partial \boldsymbol{X}_d} - \frac{\boldsymbol{r}_{bc} \cdot \boldsymbol{r}_{ba}}{||\boldsymbol{r}_{ba}||^2}\frac{\partial \theta_j}{\partial \boldsymbol{X}_c} \tag{3.40}$$

and

$$\frac{\partial \theta_j}{\partial \boldsymbol{X}_b} = \left(\frac{\boldsymbol{r}_{bc} \cdot \boldsymbol{r}_{ba}}{||\boldsymbol{r}_{ba}||^2} - 1\right)\frac{\partial \theta_j}{\partial \boldsymbol{X}_c} - \frac{\boldsymbol{r}_{da} \cdot \boldsymbol{r}_{ba}}{||\boldsymbol{r}_{ba}||^2}\frac{\partial \theta_j}{\partial \boldsymbol{X}_d}. \tag{3.41}$$

The derivative with respect to a specific coordinate component, say X_a, is obtained by extracting the corresponding component from the gradient vector $\partial\theta_j/\partial \boldsymbol{X}_a$:

$$\frac{\partial \theta_j}{\partial X_a} = \boldsymbol{e}_x^{\mathsf{T}} \frac{\partial \theta_j}{\partial \boldsymbol{X}_a}, \tag{3.42}$$

where $\boldsymbol{e}_x = [1,0,0]^{\mathsf{T}}$ denotes the unit basis vector in the x-direction. Analogous expressions hold for derivatives with respect to Y_a, Z_a, or for derivatives with respect to the coordinates of other nodes.

For the deformed configuration, we denote the dihedral angle by θ_j' and the nodal positions by $\boldsymbol{X}_a' = \boldsymbol{X}_a + \boldsymbol{u}_a$, with $\boldsymbol{u}_a = [u_a^x, u_a^y, u_a^z]^{\mathsf{T}}$ being the prescribed displacement of node a. Under displacement-controlled loading, the displacements are held fixed when taking partial derivatives with respect to nodal coordinates, hence $\partial \boldsymbol{X}_a'/\partial X_a = [1,0,0]^{\mathsf{T}}$ and consequently

$$\frac{\partial \theta_j'}{\partial X_a} = \boldsymbol{e}_x^{\mathsf{T}} \frac{\partial \theta_j'}{\partial \boldsymbol{X}_a'}. \tag{3.43}$$

For brevity, we introduce the notation

$$e_{ja} := \frac{\partial \theta_j}{\partial X_a} \quad \text{and} \quad e'_{ja} := \frac{\partial \theta_j'}{\partial X_a}. \tag{3.44}$$

Finally, substituting equation (3.36) and the angle derivatives into the chain rule (equation (3.35)) yields the sensitivity of the hinge strain energy with respect to X_a. We denote this sensitivity by I_{ja}, i.e.

$$\begin{aligned} I_{ja} &:= \frac{\partial U_{Hj}}{\partial X_a} \\ &= \frac{k_{Hj}}{2} \frac{X_a - X_d}{L_{Hj}} (\theta_j' - \theta_j)^2 + k_{Hj} L_{Hj} (\theta_j' - \theta_j)(e'_{ja} - e_{ja}) \\ &= k_{Hj}(\theta_j' - \theta_j) \left[\frac{(X_a - X_d)(\theta_j' - \theta_j)}{2L_{Hj}} + L_{Hj}(e'_{ja} - e_{ja}) \right], \end{aligned} \tag{3.45}$$

where I_{ja} represents the contribution of hinge j to the sensitivity with respect to the x-coordinate of node a.

Recall that the design vector $\boldsymbol{x} = [x_1, \ldots, x_M]^{\mathsf{T}}$ collects all nodal coordinate components, where each x_m corresponds to a specific coordinate of a particular node. The sensitivities of the bar and hinge strain energies with respect to this design variable, denoted by H_{im} and I_{jm}, are precisely the quantities derived in the preceding sections for the corresponding node and the coordinate direction. For instance, when x_m represents the x-coordinate X_p of node p, we have $H_{im} = H_{ip}$ for each bar i, where H_{ip} is given by equation (3.34). Similarly, when x_m represents the x-coordinate X_a of node a, we have $I_{jm} = I_{ja}$ for each hinge j, with I_{ja} defined in equation (3.45). For other coordinate directions or other nodes, the corresponding expressions follow analogously. The total sensitivity of the structural strain energy with respect to x_m is then obtained by summing the contributions from all elements:

$$F_m^S := \frac{\partial U}{\partial x_m} = \sum_{i=1}^{N_1} H_{im} + \sum_{j=1}^{N_2} I_{jm}, \tag{3.46}$$

where only the elements connected to the node associated with x_m contribute non-zero values; for elements not connected to that node, $H_{im} = 0$ or $I_{jm} = 0$.

(iii) Gradient-based geometry update

To minimize the strain energy with respect to nodal coordinates, we adopt a gradient descent strategy. At a given design point $\boldsymbol{x}^{(\psi)}$, a full nonlinear mechanical analysis is performed to obtain

the equilibrium displacements and the structural strain energy $U(\boldsymbol{x}^{(\psi)})$. The geometric sensitivities $F_m^S = \partial U/\partial x_m$ are then evaluated at this configuration.

Using these sensitivities, the nodal coordinates are updated along the negative normalized gradient direction with an adaptively scaled step size, while strictly enforcing the bound constraints. The detailed update scheme, including the adaptive step-size strategy, is presented in Section 4(b).

Unlike the topology optimization, which uses sensitivity information to construct an explicit approximation, the geometry optimization performs sensitivity analysis at each iteration as origami configuration updates. This ensures that the design evolution consistently follows the instant gradient of the physical strain energy landscape.

4. Optimization algorithms

This section summarizes the update schemes used to solve the topology and geometry subproblems introduced in the previous section. Specifically, we adopt the OC update for the topology variables $\boldsymbol{t}$ and the gradient-based update with adaptive step sizing for the geometric variables $\boldsymbol{x}$.

(a) Topology optimization update scheme

To update the topology design variables, we employ the OC method [89–91]. At each topology optimization iteration v, a nonlinear mechanical analysis is first performed at the current design $\boldsymbol{t}^{(v)}$ to evaluate the strain energy $U^{(v)}$ and the hinge energies $U_{Hj}^{(v)}$. The sensitivities $\partial U_{Hj}/\partial t_j$ (equation (3.12)) are then computed and used to form the coefficients $a_j^{(v)}$ in the explicit approximation (equation (3.14)).

With $a_j^{(v)}$ held fixed, the design variables are updated by an OC step with a Lagrange multiplier to satisfy both the crease-length constraint in equation (3.16) and the bound constraints $t_{\min} \le t_j \le 1$. The OC update equation is written as

$$\left.\begin{aligned} t_j^{(v+1)} &= \max(t_j^{\mathrm{L}}, \min(t_j^{\mathrm{U}}, t_j^{(v)} B_j^{(v)})), \quad j = 1, \ldots, N_2, \\ \text{and} \qquad t_j^{\mathrm{L}} &= \max(t_{\min}, t_j^{(v)} - m), \quad t_j^{\mathrm{U}} = \min(1, t_j^{(v)} + m), \end{aligned}\right\} \tag{4.1}$$

where t_j^{L} and t_j^{U} are the truncation bounds determined by the move limit m. The factor $B_j^{(v)} = -a_j^{(v)}/b_j^{(v)}$ is nonnegative because $a_j^{(v)} < 0$ for $\beta > 0$. Taking $b_j^{(v)} = \lambda^{(v)} L_{Hj}^0$, the Lagrange multiplier $\lambda^{(v)}$ is solved by bisection to enforce equation (3.16). This OC update repeats until convergence.

The topology optimization loop terminates when the following convergence criterion is satisfied:

$$\frac{|U(\boldsymbol{t}^{(v+1)}) - U(\boldsymbol{t}^{(v)})|}{\max(|U(\boldsymbol{t}^{(v)})|, |U(\boldsymbol{t}^{(v+1)})|, \epsilon)} \le \xi^{\mathrm{TO}}, \tag{4.2}$$

where ξ^{TO} is a prescribed tolerance, ϵ is a small positive number to avoid division by zero, and v is the iteration counter.

(b) Geometry optimization update scheme

The nodal coordinates are optimized using a normalized gradient descent method with adaptive step sizes. At each geometry-optimization iteration ψ, a full nonlinear mechanical analysis is first performed at the current configuration $\boldsymbol{x}^{(\psi)}$ to evaluate the strain energy $U(\boldsymbol{x}^{(\psi)})$ and the sensitivity $F_m^S = \partial U/\partial x_m$ (equation (3.19)) The design variables are then updated along the

https://royalsocietypublishing.org/journal/rspa Proc. R. Soc. A 482: 20260207

Table 1. Material parameters for the bar-and-hinge model.

k_H^B	k_H^F	A	C	α_1	α_2
1	0.01	0.2	1×10^4	5	1

negative normalized gradient direction:

$$x_m^{(\psi+1)} = x_m^{(\psi)} - \alpha^{(\psi)} \frac{F_m^S}{\|\boldsymbol{F}^S\|}, \quad m = 1, \ldots, M, \tag{4.3}$$

where $\boldsymbol{F}^S = [F_1^S, \ldots, F_M^S]^\mathsf{T}$ and the step size $\alpha^{(\psi)}$ is adaptively reduced as the major iteration proceeds:

$$\alpha^{(\psi)} = \frac{move}{\max\left(1,\, \omega - \omega_{\text{fold}}\right)}, \tag{4.4}$$

with $move = \eta \cdot \min(L_{Bi})/N_S$, where L_{Bi} is the initial length of bar i, N_S is the maximum number of shape iterations per major step, η is a scaling factor, ω is the current major iteration index, and ω_{fold} is the number of major iterations over which material properties evolve. This adaptive scaling allows larger steps in early stages for rapid exploration and finer adjustments in later stages when the design approaches a local minimum. After the update, the bound constraints $\underline{x}_m \le x_m \le \overline{x}_m$ (equation (3.19)) are enforced by projection.

In contrast to the topology optimization, the geometry optimization does not rely on a fixed sensitivity over multiple inner iterations; instead, a new sensitivity analysis is performed at every iteration. This guarantees that the update direction always reflects the exact gradient of the current energy landscape and avoids errors caused by outdated sensitivities.

The iteration terminates when the relative reduction in the actual strain energy U between successive steps falls below a prescribed tolerance ξ^{SO}:

$$\frac{U(\boldsymbol{x}^{(\psi)}) - U(\boldsymbol{x}^{(\psi+1)})}{U(\boldsymbol{x}^{(\psi)})} \le \xi^{\text{SO}}, \tag{4.5}$$

or when the maximum number of iterations N_S is reached.

5. Numerical examples

This section presents a set of numerical examples to demonstrate the effectiveness and feasibility of the proposed unified framework for non-rigid origami design. These examples demonstrate the ability of the method to generate crease patterns and deformation modes under a range of spatial constraints, boundary conditions and material parameters. The performance of the algorithm is evaluated by tracking the reduction in structural strain energy and examining the corresponding force–displacement responses. Each example highlights a different aspect of the optimization process, thereby illustrating the versatility and robustness of the proposed approach for designing origami structures with tailored properties.

All numerical examples adopt the same set of material parameters, listed in table 1. Here, k_H^B and k_H^F denote the torsional stiffness of bending and folding hinges, respectively; A is the cross-sectional area of a bar element; C represents the tangential elastic modulus of the bar; and α_1 and α_2 are parameters defining the hyperelastic constitutive model in equation (3.23).

Note that all quantities in the analysis are dimensionless; nevertheless, they are scaled consistently within a unified dimensional framework to ensure physical correctness.

The algorithmic parameters adopted for each example are summarized in table 2. These values were selected based on preliminary convergence studies and are used consistently throughout all numerical investigations. Brief remarks on the sensitivity of results to these choices are provided within each example subsection.

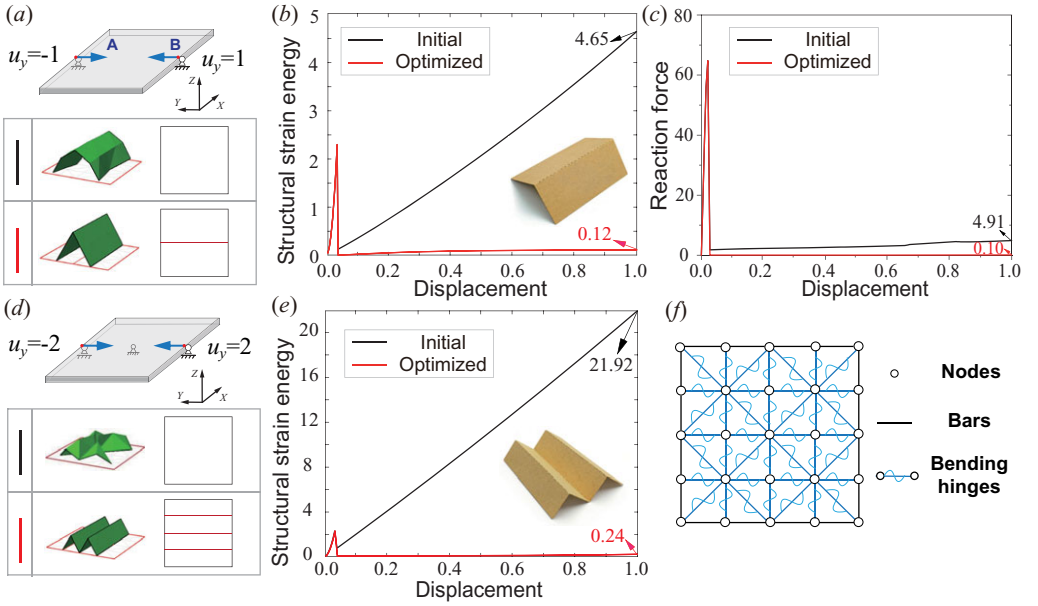

Figure 5. Mechanical responses and configurations for two straight-fold cases. (*a*) Boundary conditions and the initial/final configurations of the first example. (*b*) Strain energy versus displacement for the simple straight fold. (*c*) Reaction force versus displacement for the same case. (*d*) Optimized configuration with a fixed midpoint. (*e*) Strain energy versus displacement for the midpoint-fixed case. (*f*) Initial mesh discretization.

Table 2. Key algorithmic parameters for all numerical examples.

parameter	folds	W-bomb	substrate	Miura 1	Miura 2	Kresling
Nodes	15	25	25	9	25	96
K_f/K_b	0.001/1	0.01/1	0.01/1	$0.001 \rightarrow 0.1/1$	$0.001 \rightarrow 0.1/1$	0.01/1
E	10^4	10^4	10^4	$10^2 \rightarrow 10^4$	$10^2 \rightarrow 10^4$	10^4
Initial t	0.02	0.05	0.02	0.5	0.5	10^{-3}
$t_{\min}$	0.02	0.05	0.02	0.18	0.01	10^{-3}
Opt. dofs	y	y	x, y	x, y, z	x, y, z	x, y, z
Iterations	10	20	20	10	10	14
DispStep	100	200	200	100	100	100

(a) Straight folds

The first example considers a benchmark problem with a known solution, namely a simple straight fold. The boundary conditions are prescribed as follows (figure 5a): point A is constrained in the y- and z-directions and subjected to a displacement $u_x = 1$; point B is subject to the same constraints and prescribed displacement $u_x = -1$. The initial mesh discretization is shown in figure 5f. We compare the mechanical response before and after optimization. The strain energy and reaction force, plotted as functions of displacement in figure 5b,c, show that at equilibrium the strain energy decreases from 4.65 to 0.12 and the final reaction force drops from 4.91 to 0.10. This pronounced reduction in both quantities demonstrates the effectiveness of the proposed method in transforming a high-energy folded state into a stable, low-energy configuration.

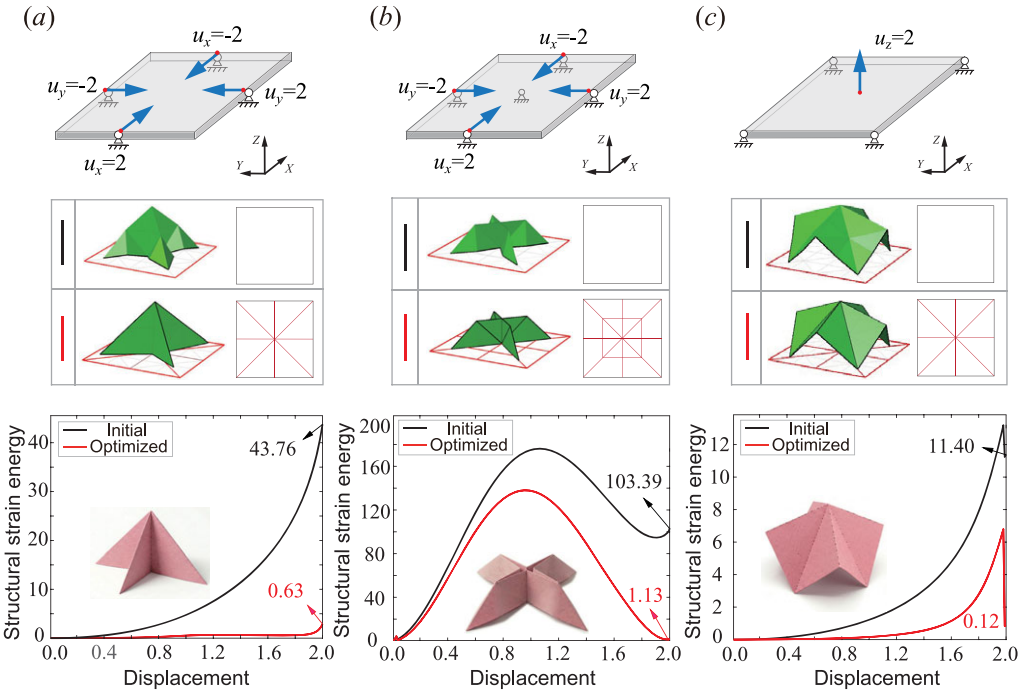

Figure 6. Waterbomb-base formation under three boundary conditions. (*a*) Edge-midpoint inward displacements with free centre. (*b*) Edge-midpoint inward displacements with fixed centre. (*c*) Vertices constrained in the *z*-direction plus a central upward displacement.

When the membrane centre is additionally fixed and a uniform vertical displacement is applied along the top and bottom edges, the optimization drives the structure to evolve into a distinct pattern of three parallel folds (figure 5d). This reduces the final equilibrium strain energy from 21.92 to 0.24 (figure 5e). The final single-crease and three-crease patterns were found to be insensitive to the initial topology variable for $t_{\min} \in [0.01, 0.05]$ and to the move limit within ±50% of the reported value; only the number of inner iterations required for convergence was affected.

(b) Waterbomb base and its variants

Building on the baseline straight-fold case above, we next demonstrate how spatial constraints can steer crease evolution towards distinct low-energy topologies. We investigate the formation of waterbomb-base patterns on a square thin plate under three boundary conditions, as illustrated schematically in figure 6. In case (a), inward prescribed displacements are applied at the midpoints of the four edges, and each midpoint is constrained to move only along its corresponding coordinate axis; the centre point remains free. In case (b), the same edge displacements are applied, but the centre point is fully fixed. In case (c), the four vertices are constrained in the *z*-direction, and an upward displacement is applied at the centre along the positive *z*-direction.

Despite these differences, cases (a) and (c) evolve into the same symmetric waterbomb-base crease pattern (figure 6, left and right columns). In contrast, case (b) yields a qualitatively different and more intricate pattern—a variant of the waterbomb base—because fixing the centre point breaks the rotational symmetry.

Two key observations can be drawn from these results. First, the convergence of two different loading paths (cases (a) and (c)) to an identical low-energy crease pattern suggests that the proposed framework can discover mechanically optimal topologies that are not tied to a specific

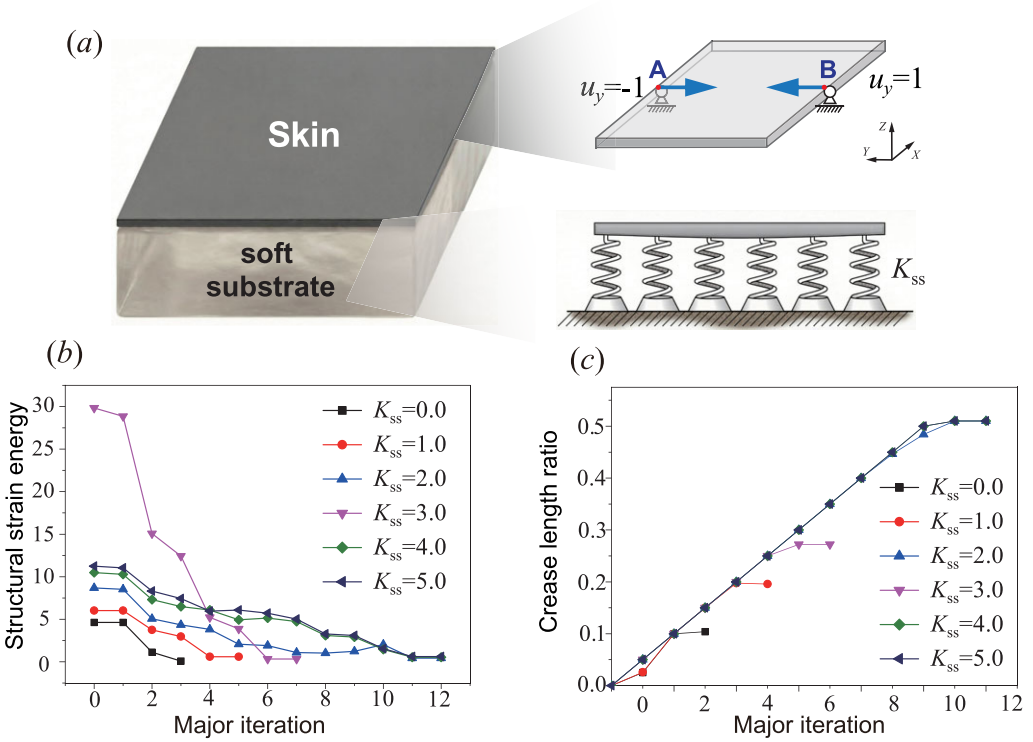

Figure 7. Influence of substrate stiffness on optimized patterns in a bilayer system. (*a*) Schematic of the bilayer structure comprising a stiff skin bonded to a soft substrate, where the substrate is represented by an equivalent linear spring. (*b*) Evolution of structural strain energy during optimization. (*c*) Evolution of total crease-length ratio during optimization.

load application. Second, the dramatic change induced by fixing the centre point (case (b)) highlights the decisive role of spatial constraints, as a single additional constraint can force the optimization to converge to a different local minimum. All three boundary-condition variants employed the identical set of algorithmic parameters, and the converged symmetric patterns remained unchanged when the move limit and convergence tolerance were perturbed by ±50% around their nominal values.

(c) Optimized patterns on a soft substrate

To further enrich the design space, we introduce an additional physical constraint by coupling the thin-walled skin to a compliant substrate. Bilayer systems consisting of a relatively stiff skin bonded to a soft substrate are common in nature, for example in plant seeds and human skin. Under simple loading, the compliant substrate can trigger buckling of the planar skin into complex three-dimensional shapes with rich topological features [78,92]. In our model, the substrate is represented by an equivalent linear spring, as illustrated in figure 7a. The thin-walled skin is discretized using the initial bar-and-hinge model (figure 5f), and the material parameters are listed in table 1. The boundary conditions are the same as those in §5a.

This subsection investigates how the substrate stiffness, denoted by K_{ss}, influences the optimized patterns emerging from the bilayer system. As shown in figure 8, distinct crease patterns emerge in the thin-walled skin during the optimization process, and the global deformation progressively localizes along these creases. Specifically, the optimized structure develops one, two and three straight creases when $K_{ss} = 0$, 1 and 3, respectively. For other values, such as $K_{ss} = 2, 4$ and 5, both the final deformation and the crease layout become more intricate.

The substrate stiffness is a key factor governing the final optimized configuration of the thin-walled skin under the prescribed displacements. As K_{ss} increases, the deformation becomes more

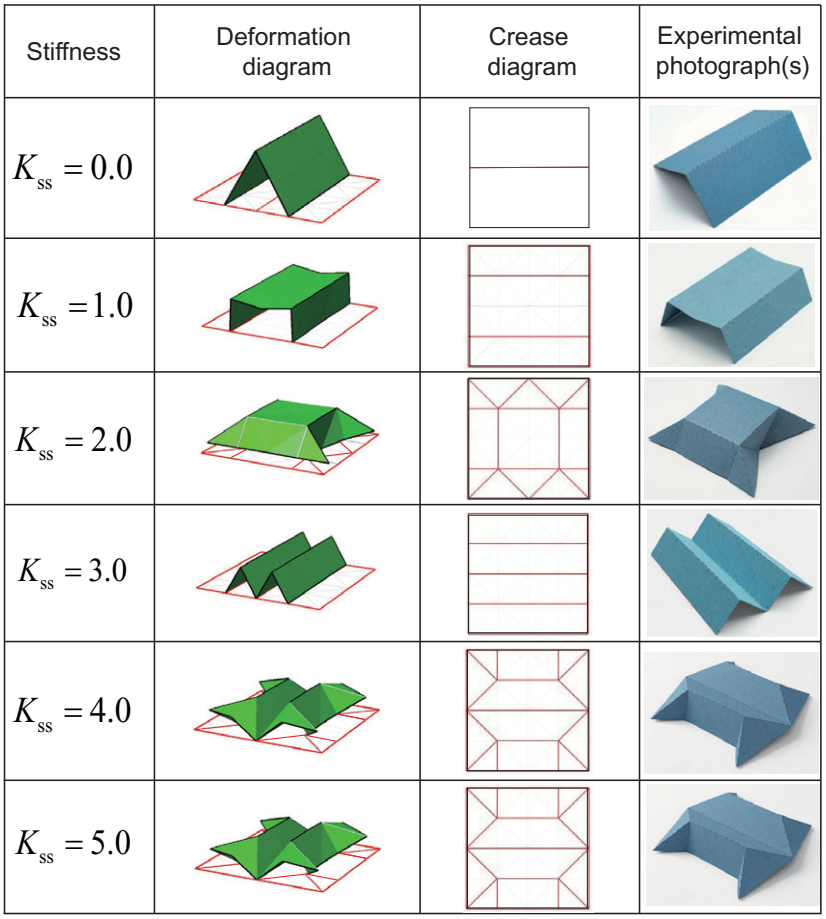

Figure 8. Comparison of optimized deformation geometries, crease patterns and experimental prototypes under varying substrate stiffness K_{ss}.

complex, and the total crease-length ratio generally increases. When $K_{ss} > 3$, the initial and final deformation patterns differ markedly.

This transition can be physically interpreted through the interplay between localized folding and the restoring force of the substrate. When $K_{ss} = 0$, the structure accommodates compression via a single long-wave fold that minimizes panel bending. As K_{ss} increases, the substrate penalizes large out-of-plane displacements, making a deep fold energetically unfavourable and driving the redistribution of deformation into multiple shallower folds—hence the increase from one to three creases as K_{ss} grows from 0 to 3. For $K_{ss} > 3$, the plate develops a distributed, multi-crease pattern analogous to short-wavelength wrinkling instabilities in thin films on compliant substrates [78,92], where the wrinkle wavelength is governed by the competition between film bending energy and substrate elastic energy. All values of K_{ss} were tested with the same optimization parameters (table 2), confirming that the crease-pattern transition is mechanically driven rather than algorithmically induced.

(d) Miura-ori pattern

Next, we consider a non-planar benchmark to further demonstrate that the proposed method can recover classical rigid-foldable patterns from an initially uniform mesh. The optimization starts from a pre-deformed state obtained by applying a small out-of-plane displacement to a flat

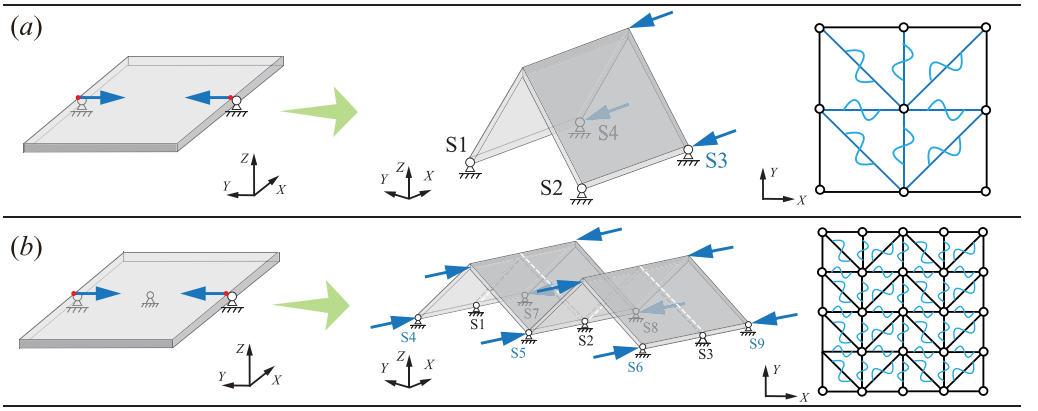

Figure 9. (*a*) Boundary conditions and mesh for a single Miura-ori unit. Points S1 and S2 are fixed in the *x*- and *z*-directions, S3 is fixed in the *y*- and *z*-directions and S4 is fixed only in the *z*-direction. (*b*) Boundary conditions and mesh for a 2 × 2 Miura-ori assembly. Points S1 and S2 are fixed in *x* and *z*; S3 is fully fixed; S4, S5, S7 and S8 are fixed in *y* and *z*; and S6 and S9 are fixed in *y* and *z*.

sheet. The resulting configuration forms a single-unit Miura-ori pattern and exhibits nearly ideal rigid-foldable behaviour. Figure 9a shows the boundary conditions and initial mesh for a single Miura-ori unit. Points S1 and S2 are constrained in the *x*- and *z*-directions, S3 is constrained in the *y*- and *z*-directions and S4 is constrained only in the *z*-direction.

Under displacement-controlled loading, the strain energy is dominated by the folding component, while the tensile contribution remains low and the bending contribution is negligible (figure 10a). This indicates that deformation localizes primarily along the creases and induces minimal panel distortion.

A comparative analysis (figure 10b) shows a 97.0% reduction in the final strain energy, from 8.48 to 0.25, and an 86.5% decrease in the average strain energy over the full displacement range.

Figure 10c shows the evolution of strain energy during the optimization. After an initial increase, the strain energy decreases over the main iterations and eventually stabilizes, reflecting the gradual emergence of a well-defined Miura-ori crease pattern from the initially uniform mesh.

The force–displacement curves in figure 10d indicate a 75.7% reduction in the maximum reaction force and an 88.9% decrease in the average reaction force. These results show that the optimized structure requires substantially less external work to achieve the same deformation. These results demonstrate the ability of the proposed framework to generate low-energy, mechanically efficient origami structures through combined topology and geometry optimization. For this example, a neutral initial topology variable ($t = 0.5$) and a V-shaped geometric imperfection were adopted to steer the optimization towards the expected rigid-foldable Miura-ori pattern. When the geometric perturbation was removed, the algorithm still converged to a low-energy folded configuration, albeit with a slightly different crease topology, indicating that the initial geometric cue provides a mild but not indispensable bias.

Under symmetric compression about its median plane, a pre-folded W-shaped structure, whose initial configuration is shown in figure 9b, evolves into a multi-cell Miura-ori pattern. The optimized configuration exhibits substantial improvements in mechanical performance, with notable reductions in both the total strain energy and the support reaction forces, as illustrated in figure 11a,b.

The evolution of the relative contributions of each optimization strategy, as well as the corresponding changes in efficiency throughout the iterative process, is shown in figure 11c,d.

The optimization follows a clear three-phase evolution. The first phase is dominated by geometry optimization, which rapidly improves performance through geometric adjustments.

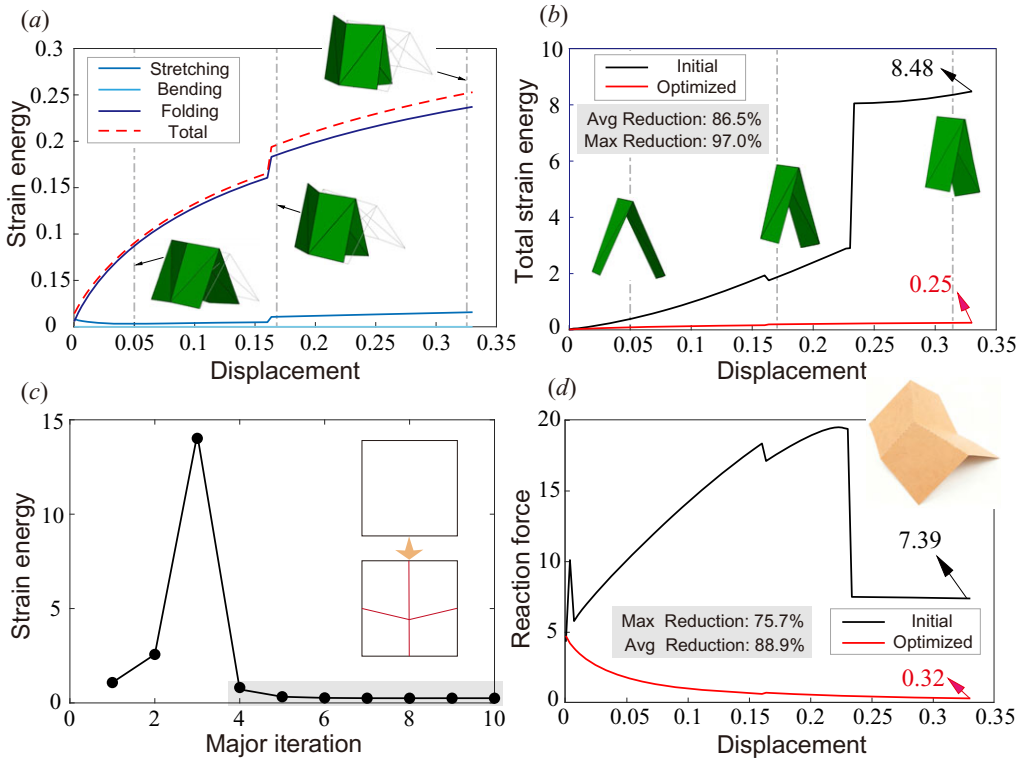

Figure 10. Optimization analysis for a single Miura-ori unit. (*a*) Strain-energy distribution in the optimized structure. (*b*) Comparison of strain energy before and after optimization. (*c*) Convergence history of strain energy. (*d*) Force–displacement responses before and after optimization.

In the second phase, topology optimization plays an increasingly important role by reorganizing the load paths. In the final phase, geometry optimization again takes the lead to refine the local geometry within the fixed topological framework. The final contribution ratios confirm both the dominant role of topology optimization and the complementary role of geometry optimization in achieving the optimal design. The gradual activation of Young's modulus (from 10^2 to 10^4) and the folding stiffness over the first five major iterations was found to be essential: when this continuation strategy was omitted, the optimization prematurely converged to a local minimum with a final strain energy approximately three times higher. Among all algorithmic parameters, the material continuation schedule proved to be the most influential for this example.

(e) Kresling tube origami

We consider a classical benchmark: a Kresling tube origami subjected to torsion. The geometry and boundary conditions are shown in figure 12a. A prescribed twist of 0.2 rad is imposed at the top edge, while the bottom edge is fully fixed. To exploit cylindrical symmetry, the sensitivity analysis and nodal updates for geometry optimization are formulated directly in cylindrical coordinates.

Figure 12c shows the strain energy as a function of displacement during loading, revealing the characteristic multi-stability of the Kresling pattern. The structure transitions from an initial stable state (state 1) to a second stable state (state 2) by crossing an energy barrier, confirming that large deformations can access multiple equilibrium paths.

The evolution of the crease pattern and the corresponding reduction in strain energy are shown in figure 12d. A spiral crease pattern emerges near the centre and gradually develops into a complete Kresling spiral. The total strain energy drops sharply from 712.3 to 5.8.

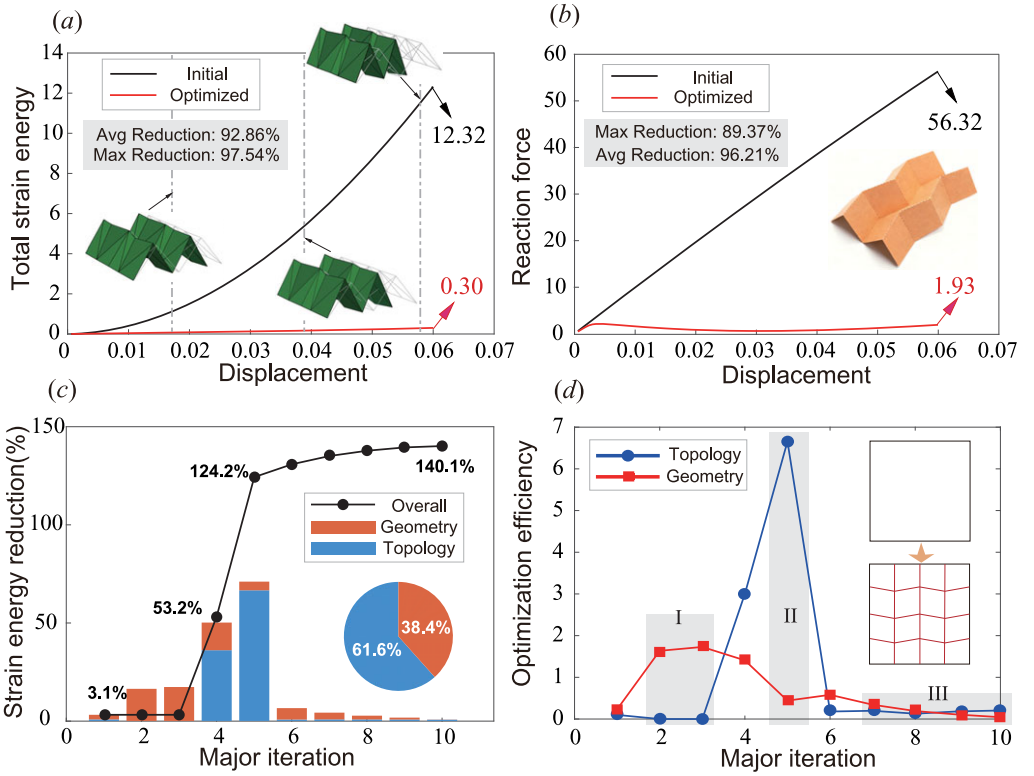

Figure 11. Optimization analysis for a 2 × 2 Miura-ori assembly. (*a*) Comparison of strain energy before and after optimization. (*b*) Reaction force versus displacement response. (*c*) Evolution of cumulative contributions from each optimization method. (*d*) Efficiency evolution of individual strategies and crease emergence.

Figure 12e shows the relative contributions of geometry and topology optimization throughout the iterative process. Geometry optimization dominates the initial iterations: nodal adjustments relax geometric constraints and produce a rapid drop in strain energy. A clear low-energy crease pattern subsequently emerges. The contribution of topology optimization then increases as bending hinges are systematically converted into folding hinges in regions of high strain energy, stabilizing and refining the characteristic Kresling spiral. The final contribution ratio, measured in terms of strain-energy reduction, is approximately 65% from geometry optimization and 35% from topology optimization. This complementary process allows an efficient crease pattern to evolve from a uniform initial mesh without relying on a predefined template. The characteristic spiral crease pattern emerged robustly for $t_{\min} \in [10^{-3}, 10^{-2}]$, and the final topology was insensitive to further tightening of the convergence tolerance. The adoption of cylindrical-coordinate sensitivity analysis and adaptive displacement loading was critical for preserving mesh quality during the large torsional deformation; without these measures, element distortion near the loaded edge occasionally terminated the optimization prematurely.

6. Conclusion

This paper proposes a unified computational design framework for the concurrent topology and geometry optimization of origami structures under spatial constraints, based on strain-energy minimization. The framework couples the nonlinear bar-and-hinge model with gradient-based optimization to simulate load-driven crease evolution in thin-walled systems. By directly minimizing structural strain energy under prescribed displacements, the proposed approach

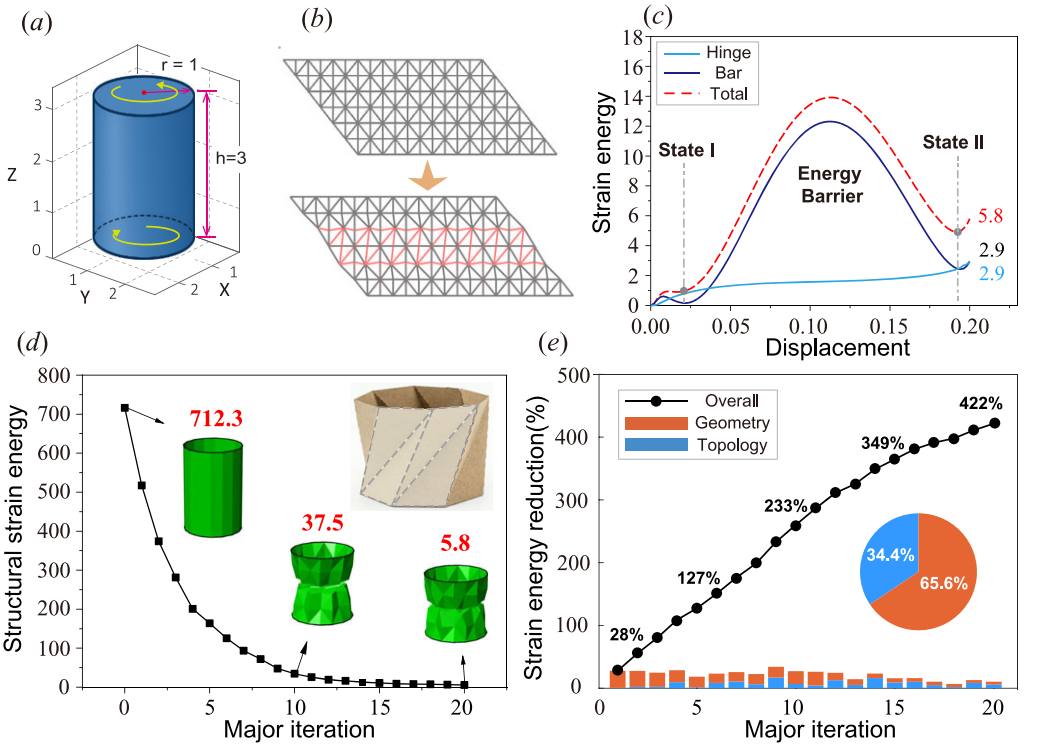

Figure 12. Optimization of a Kresling tube origami. (*a*) Geometry and boundary conditions. (*b*) Unfolded initial mesh and optimized mesh. (*c*) Strain energy–displacement response showing bistability. (*d*) Evolution of the total strain energy during optimization. (*e*) Cumulative contributions of geometry and topology optimization to the strain energy reduction.

generates low-energy folded configurations across multiple geometries and boundary conditions, including straight folds, waterbomb-base patterns, Miura-ori patterns and a Kresling-type cylindrical origami.

The proposed framework consistently achieves substantial reductions in structural strain energy and reaction forces, transforming high-energy deformation modes into stable, low-energy folded states. Across the numerical examples, the reduction in strain energy typically exceeds 90%. For example, the strain energy of a single Miura-ori unit decreases from 8.48 to 0.25, corresponding to a 97.1% reduction.

Robust crease evolution relies on the concurrent use of topology and geometry optimization. Topology optimization identifies favourable crease locations by switching hinges between bending- and folding-dominated behaviour, whereas geometry optimization adjusts nodal positions to improve geometric compatibility and mitigate mesh dependence. The combination enables complex, mechanically efficient crease patterns to emerge without relying on predefined templates.

The final crease morphology depends strongly on the imposed boundary conditions and loading path. The waterbomb-base examples show that different constraints can lead to distinct low-energy patterns, while different loading histories may converge to the same pattern if they reach the same energy minimum. These results highlight both the adaptability of the framework and the role of spatial constraints in shaping the energy landscape of foldable structures.

The optimization problem is non-convex, and the final pattern can be sensitive to several inputs. Regular, sufficiently fine meshes provide a less biased starting point, and the examples demonstrate that quasi-structured meshes consistently yield physically meaningful low-energy patterns. Algorithmic parameters such as the move limit and convergence tolerances offer a

robust balance across the studied cases; to reduce manual tuning, these limits can be adaptively adjusted when oscillations are detected. The current framework adopts a displacement-controlled loading scheme, which simplifies the sensitivity analysis; extension to force-controlled loading via the adjoint method is conceptually straightforward. The method converges to a local minimum determined by the initial geometry, material properties and loading sequence; identical inputs yield reproducible designs, while different loading paths may lead to distinct optima, reflecting the path-dependent physics of folding. Future extensions include dynamic loading, multi-material systems and manufacturability constraints, further bridging computational origami design with applications in metamaterials, soft robotics and deployable structures.

Ethics. This work did not involve any active collection of human or animal data, as it is entirely based on computational simulations. No ethical approval was required.

Data accessibility. This work does not have any experimental data. All computational results presented in the figures are reproducible using the methods described in the manuscript. The MERLIN2 software is available at www2.coe.pku.edu.cn/faculty/liuke/downloads.html.

The data are provided in the electronic supplementary material [93].

Declaration of AI use. We have not used AI-assisted technologies in creating this article.

Authors' contributions. Y.T.: data curation, formal analysis, investigation, methodology, visualization, writing—original draft, writing—review and editing; W.W.: data curation, formal analysis, investigation, methodology, visualization, writing—original draft; H.D.: conceptualization, funding acquisition, writing—review and editing; K.L.: conceptualization, funding acquisition, investigation, methodology, project administration, supervision, writing—review and editing.

All authors gave final approval for publication and agreed to be held accountable for the work performed therein.

Conflict of interest declaration. We declare we have no competing interests.

Funding. This work was supported by the National Natural Science Foundation of China through grants 12588301, 12202008 and 12372159.

Acknowledgements. The authors acknowledge the High-Performance Computing Platform at Peking University for providing computational resources.

Disclaimer. The information provided in this paper is the sole opinion of the authors and does not necessarily reflect the views of the sponsoring agencies.

References

1. Lang RJ. 2012 *Origami design secrets: mathematical methods for an ancient art*. Boca Raton, FL: CRC Press.
2. Lang RJ. 1996 A computational algorithm for origami design. In *Proceedings of the Twelfth Annual Symposium on Computational Geometry*, Philadelphia, PA, pp. 98–105. New York, NY: ACM.
3. Silverberg JL, Evans AA, McLeod L, Hayward RC, Hull T, Santangelo CD, Cohen I. 2014 Using origami design principles to fold reprogrammable mechanical metamaterials. *Science* **345**, 647–650. (doi:10.1126/science.1252876)
4. Schenk M, Guest SD. 2011 Origami folding: a structural engineering approach. *Origami* **5**, 291–304.
5. Turner N, Goodwine B, Sen M. 2016 A review of origami applications in mechanical engineering. *Proc. Inst. Mech. Eng. C: J. Mech. Eng. Sci.* **230**, 2345–2362. (doi:10.1177/0954406215597713)
6. Meloni M, Cai J, Zhang Q, Sang-Hoon Lee D, Li M, Ma R, Parashkevov TE, Feng J. 2021 Engineering origami: a comprehensive review of recent applications, design methods, and tools. *Adv. Sci.* **8**, 2000636. (doi:10.1002/advs.202000636)
7. Misseroni D, Pratapa PP, Liu K, Kresling B, Chen Y, Daraio C, Paulino GH. 2024 Origami engineering. *Nat. Rev. Methods Primers* **4**, 40. (doi:10.1038/s43586-024-00313-7)
8. Yasuda H, Yang J. 2015 Reentrant origami-based metamaterials with negative Poisson's ratio and bistability. *Phys. Rev. Lett.* **114**, 185502. (doi:10.1103/PhysRevLett.114.185502)
9. Meng F, Chen S, Zhang W, Ou P, Zhang J, Chen C, Song J. 2021 Negative Poisson's ratio in graphene Miura origami. *Mech. Mater.* **155**, 103774. (doi:10.1016/j.mechmat.2021.103774)

10. Zhou Y, Jiang D, Wang L, Xiang P, Jia LJ. 2024 Cushioning performance of origami negative Poisson's ratio honeycomb steel structure. *Thin-Walled Struct.* **204**, 112284. (doi:10.1016/j.tws.2024.112284)
11. Waitukaitis S, Menaut R, Chen BGG, Van Hecke M. 2015 Origami multistability: from single vertices to metasheets. *Phys. Rev. Lett.* **114**, 055503. (doi:10.1103/PhysRevLett.114.055503)
12. Lu L, Dang X, Feng F, Lv P, Duan H. 2022 Conical Kresling origami and its applications to curvature and energy programming. *Proc. R. Soc. A* **478**, 20210712. (doi:10.1098/rspa.2021.0712)
13. Xi K, Chai S, Ma J, Chen Y. 2023 Multi-stability of the extensible origami structures. *Adv. Sci.* **10**, 2303454. (doi:10.1002/advs.202303454)
14. Zhai Z, Wang Y, Jiang H. 2018 Origami-inspired, on-demand deployable and collapsible mechanical metamaterials with tunable stiffness. *Proc. Natl Acad. Sci. USA* **115**, 2032–2037. (doi:10.1073/pnas.1720171115)
15. Filipov ET, Paulino GH, Tachi T. 2019 Deployable sandwich surfaces with high out-of-plane stiffness. *J. Struct. Eng.* **145**, 04018244. (doi:10.1061/(ASCE)ST.1943-541X.0002240)
16. Han H, Sorokin V, Tang L, Cao D. 2022 Lightweight origami isolators with deployable mechanism and quasi-zero-stiffness property. *Aerosp. Sci. Technol.* **121**, 107319. (doi:10.1016/j.ast.2021.107319)
17. Li Y, You Z. 2019 Open-section origami beams for energy absorption. *Int. J. Mech. Sci.* **157**, 741–757. (doi:10.1016/j.ijmecsci.2019.05.006)
18. Khazaaleh S, Dalaq AS, Daqaq MF. 2024 An origami-inspired energy absorber. *Smart Mater. Struct.* **33**, 045029. (doi:10.1088/1361-665X/ad3361)
19. Gao J, McShane G. 2025 Energy absorbing properties of open-celled origami-inspired mechanical metamaterials. *Int. J. Solids Struct.* **321**, 113585. (doi:10.1016/j.ijsolstr.2025.113585)
20. Lang RJ. 2009 Mathematical methods in origami design. In *Proceedings of Bridges 2009: Mathematics, Music, Art, Architecture, Culture, Banff, Alberta, Canada*, pp. 11–20. St Albans, UK: Tarquin Publications.
21. Tachi T. 2013 Designing freeform origami tessellations by generalizing Resch's patterns. *J. Mech. Des.* **135**, 111006. (doi:10.1115/1.4025389)
22. Demaine E, Tachi T. 2017 Origamizer: a practical algorithm for folding any polyhedron. In *33rd Int. Symp. on Computational Geometry, SoCG 2017, Brisbane, Australia*. Wadern, Germany: Schloss Dagstuhl – Leibniz-Zentrum für Informatik.
23. Dudte LH, Vouga E, Tachi T, Mahadevan L. 2016 Programming curvature using origami tessellations. *Nat. Mater.* **15**, 583–588. (doi:10.1038/nmat4540)
24. Hu Y, Zhou Y, Liang H. 2021 Constructing rigid-foldable generalized Miura-ori tessellations for curved surfaces. *J. Mech. Robot.* **13**, 011017. (doi:10.1115/1.4048630)
25. Dang X, Feng F, Plucinsky P, James RD, Duan H, Wang J. 2022 Inverse design of deployable origami structures that approximate a general surface. *Int. J. Solids Struct.* **234**, 111224. (doi:10.1016/j.ijsolstr.2021.111224)
26. Tachi T. 2013 Freeform origami tessellations by generalizing Resch's patterns. In *International Design Engineering Technical Conferences and Computers and Information in Engineering Conference, Portland, OR*, vol. 55942, p. V06BT07A025. New York, NY: American Society of Mechanical Engineers.
27. Reeger J, Fornberg B, Watts M. 2016 Numerical quadrature over smooth, closed surfaces. *Proc. R. Soc. A* **472**, 20160401. (doi:10.1098/rspa.2016.0401)
28. Yu Y, Chen Y, Paulino G. 2023 Programming curvatures by unfolding of the triangular Resch pattern. *Int. J. Mech. Sci.* **238**, 107861. (doi:10.1016/j.ijmecsci.2022.107861)
29. Sharma H, Upadhyay SH. 2021 Folding pattern design and deformation behavior of origami based conical structures. *Adv. Space Res.* **67**, 2058–2076. (doi:10.1016/j.asr.2021.01.012)
30. Sharma H, Chaudhary A, Upadhyay S. 2023 Experimental verification of the bistable behavior of conical Kresling origami. *Thin-Walled Struct.* **190**, 110980. (doi:10.1016/j.tws.2023.110980)
31. Delimont IL, Magleby SP, Howell LL. 2015 Evaluating compliant hinge geometries for origami-inspired mechanisms. *J. Mech. Robot.* **7**, 011009. (doi:10.1115/1.4029325)
32. Peng R, Chirikjian GS. 2025 Thick-panel origami structures forming seamless surfaces. *Nat. Commun.* **16**, 3881. (doi:10.1038/s41467-025-59141-2)
33. Feng F, Dang X, James RD, Plucinsky P. 2020 The designs and deformations of rigidly and flat-foldable quadrilateral mesh origami. *J. Mech. Phys. Solids* **142**, 104018. (doi:10.1016/j.jmps.2020.104018)

34. Cai J, Ren Z, Ding Y, Deng X, Xu Y, Feng J. 2017 Deployment simulation of foldable origami membrane structures. *Aerosp. Sci. Technol.* **67**, 343–353. (doi:10.1016/j.ast.2017.04.002)
35. Wang C, Guo H, Liu R, Deng Z. 2022 A programmable origami-inspired space deployable structure with curved surfaces. *Eng. Struct.* **256**, 113934. (doi:10.1016/j.engstruct.2022.113934)
36. Yue S. 2023 A review of origami-based deployable structures in aerospace engineering. *J. Phys.: Conf. Ser.* **2459**, 012137.
37. Fuchi K, Buskohl PR, Bazzan G, Durstock MF, Reich GW, Vaia RA, Joo JJ. 2016 Design optimization challenges of origami-based mechanisms with sequenced folding. *J. Mech. Robot.* **8**, 051011. (doi:10.1115/1.4032442)
38. Dang X, Lu L, Duan H, Wang J. 2022 Deployment kinematics of axisymmetric Miura origami: unit cells, tessellations, and stacked metamaterials. *Int. J. Mech. Sci.* **232**, 107615. (doi:10.1016/j.ijmecsci.2022.107615)
39. Fang H, Chu SCA, Xia Y, Wang KW. 2018 Programmable self-locking origami mechanical metamaterials. *Adv. Mater.* **30**, 1706311. (doi:10.1002/adma.201706311)
40. Ye H, Liu Q, Cheng J, Li H, Jian B, Wang R, Sun Z, Lu Y, Ge Q. 2023 Multimaterial 3D printed self-locking thick-panel origami metamaterials. *Nat. Commun.* **14**, 1607. (doi:10.1038/s41467-023-37343-w)
41. Liu K, Pratapa PP, Misseroni D, Tachi T, Paulino GH. 2022 Triclinic metamaterials by tristable origami with reprogrammable frustration. *Adv. Mater.* **34**, 2107998. (doi:10.1002/adma.202107998)
42. Kuribayashi K, Tsuchiya K, You Z, Tomus D, Umemoto M, Ito T, Sasaki M. 2006 Self-deployable origami stent grafts as a biomedical application of Ni-rich TiNi shape memory alloy foil. *Mater. Sci. Eng.: A* **419**, 131–137. (doi:10.1016/j.msea.2005.12.016)
43. Johnson M, Chen Y, Hovet S, Xu S, Wood B, Ren H, Tokuda J, Tse ZTH. 2017 Fabricating biomedical origami: a state-of-the-art review. *Int. J. Comput. Assist. Radiol. Surg.* **12**, 2023–2032. (doi:10.1007/s11548-017-1545-1)
44. Wu J *et al.* 2025 Origami-kirigami structures and its applications in biomedical devices. *Biomed. Mater. Dev.* **3**, 45–61.
45. Chen W, Wang R, Liu K. 2024 Active compliant mechanisms for optimized actuation by LCE-based artificial muscles. *Mech. Mater.* **189**, 104879. (doi:10.1016/j.mechmat.2023.104879)
46. Felton S, Tolley M, Demaine E, Rus D, Wood R. 2014 A method for building self-folding machines. *Science* **345**, 644–646. (doi:10.1126/science.1252610)
47. Chen Q, Feng F, Lv P, Duan H. 2022 Origami spring-inspired shape morphing for flexible robotics. *Soft Robot.* **9**, 798–806. (doi:10.1089/soro.2021.0030)
48. Feng Y, Yan W, Song J, Hong Z, Qiu H, Cui K, Song X, Tan J. 2024 Origami-inspired reconfigurable soft actuators for soft robotic applications. *Adv. Mater. Technol.* **9**, 2301924. (doi:10.1002/admt.202301924)
49. Lobkovsky A, Gentges S, Li H, Morse D, Witten TA. 1995 Scaling properties of stretching ridges in a crumpled elastic sheet. *Science* **270**, 1482–1485. (doi:10.1126/science.270.5241.1482)
50. Filipov E, Liu K, Tachi T, Schenk M, Paulino GH. 2017 Bar and hinge models for scalable analysis of origami. *Int. J. Solids Struct.* **124**, 26–45. (doi:10.1016/j.ijsolstr.2017.05.028)
51. Liu K, Paulino GH. 2017 Nonlinear mechanics of non-rigid origami: an efficient computational approach. *Proc. R. Soc. A* **473**, 20170348. (doi:10.1098/rspa.2017.0348)
52. Tan B, Liu K. 2024 Quantized energy absorption of sandwiched origami ring. *Extr. Mech. Lett.* **70**, 102183. (doi:10.1016/j.eml.2024.102183)
53. Wen Z, Lv P, Feng F, Duan H. 2024 A generalized geometric mechanics theory for multi-curve-fold origami: vertex constrained universal configurations. *J. Mech. Phys. Solids* **192**, 105829. (doi:10.1016/j.jmps.2024.105829)
54. Wang L, Feng F. 2026 A continuum mechanics approach for the deformation of non-Euclidean origami generated by piecewise constant nematic director fields. *J. Mech. Phys. Solids* **208**, 106460. (doi:10.1016/j.jmps.2025.106460)
55. Wang W, Liu K, Wu M, Li H, Lv P, Duan H. 2023 Instability-induced origami design by topology optimization. *Acta Mech. Sol. Sin.* **36**, 506–513. (doi:10.1007/s10338-023-00392-1)
56. Cretella V, Sohouli A, Pagani A, Suleman A. 2024 Linear and nonlinear topology optimization of origami structures based on crease pattern and axial rigidity. *Struct. Multidiscipl. Optim.* **67**, 78. (doi:10.1007/s00158-024-03773-3)
57. Martínez-Martín F, Thrall A. 2014 Honeycomb core sandwich panels for origami-inspired deployable shelters: multi-objective optimization for minimum weight and maximum energy efficiency. *Eng. Struct.* **69**, 158–167.

58. Wang S, Peng Y, Wang T, Chen X, Hou L, Zhang H. 2019 The origami inspired optimization design to improve the crashworthiness of a multi-cell thin-walled structure for high speed train. *Int. J. Mech. Sci.* **159**, 345–358. (doi:10.1016/j.ijmecsci.2019.06.017)
59. Zhang W, Ahmed S, Hong J, Ounaies Z, Frecker M. 2022 A two-stage design optimization framework for multifield origami-inspired structures. *J. Intell. Mater. Syst. Struct.* **33**, 46–69. (doi:10.1177/1045389X211011659)
60. Liu Z, Fang H, Xu J, Wang KW. 2023a Cellular automata inspired multistable origami metamaterials for mechanical learning. *Adv. Sci.* **10**, 2305146. (doi:10.1002/advs.202305146)
61. Liu Z, Fang H, Xu J, Wang KW. 2023 Digitized design and mechanical property reprogrammability of multistable origami metamaterials. *J. Mech. Phys. Solids* **173**, 105237. (doi:10.1016/j.jmps.2023.105237)
62. Fuchi K, Buskohl PR, Bazzan G, Durstock MF, Reich GW, Vaia RA, Joo JJ. 2015 Origami actuator design and networking through crease topology optimization. *J. Mech. Des.* **137**, 091401. (doi:10.1115/1.4030876)
63. Gillman AS, Fuchi K, Buskohl PR. 2019 Discovering sequenced origami folding through nonlinear mechanics and topology optimization. *J. Mech. Des.* **141**, 041401. (doi:10.1115/1.4041782)
64. Shende S, Gillman A, Yoo D, Buskohl P, Vemaganti K. 2021 Bayesian topology optimization for efficient design of origami folding structures. *Struct. Multidiscipl. Optim.* **63**, 1907–1926. (doi:10.1007/s00158-020-02787-x)
65. Chalapat K, Chekurov N, Jiang H, Li J, Parviz B, Paraoanu G. 2013 Self-organized origami structures via ion-induced plastic strain. *Adv. Mater.* **25**, 91–95. (doi:10.1002/adma.201202549)
66. Bae HJ, Bae S, Yoon J, Park C, Kim K, Kwon S, Park W. 2017 Self-organization of maze-like structures via guided wrinkling. *Sci. Adv.* **3**, e1700071. (doi:10.1126/sciadv.1700071)
67. Yan Z *et al.* 2016 Controlled mechanical buckling for origami-inspired construction of 3D microstructures in advanced materials. *Adv. Funct. Mater.* **26**, 2629–2639. (doi:10.1002/adfm.201504901)
68. Kofod G, Wirges W, Paajanen M, Bauer S. 2007 Energy minimization for self-organized structure formation and actuation. *Appl. Phys. Lett.* **90**, 081916. (doi:10.1063/1.2695785)
69. Nabika H. 2025 Structural selection rules in self-assembly and self-organization: role of entropy production rate. *Bull. Chem. Soc. Jpn.* **98**, uoaf048. (doi:10.1093/bulcsj/uoaf048)
70. Wang Y, Liu K. 2023 Shape optimization of non-rigid origami leading to emerging bistability. *Mech. Res. Commun.* **132**, 104165. (doi:10.1016/j.mechrescom.2023.104165)
71. Mahadevan L, Rica S. 2005 Self-organized origami. *Science* **307**, 1740–1740. (doi:10.1126/science.1105169)
72. Chen X, Yin J. 2010 Buckling patterns of thin films on curved compliant substrates with applications to morphogenesis and three-dimensional micro-fabrication. *Soft Matter* **6**, 5667–5680. (doi:10.1039/c0sm00401d)
73. Zhang Y, Wang F, Ma Y, Feng X. 2019 Buckling configurations of stiff thin films tuned by micro-patterns on soft substrate. *Int. J. Solids Struct.* **161**, 55–63. (doi:10.1016/j.ijsolstr.2018.11.004)
74. Kresling B, Abel JF. 2008 Natural twist buckling in shells: from the hawkmoth's bellows to the deployable Kresling-pattern and cylindrical Miura-ori. In *Proceedings of the 6th Int. Conf. on Computation of Shell and Spatial Structures, Ithaca, NY*, vol. 11, pp. 12–32. Ithaca, NY: International Association for Shell and Spatial Structures.
75. Khoddam S, Beladi H, Hodgson P, Zarei-Hanzaki A. 2014 Surface wrinkling of the twinning induced plasticity steel during the tensile and torsion tests. *Mater. Des.* **60**, 146–152. (doi:10.1016/j.matdes.2014.03.063)
76. Wang FF, Wang T, Zhang X, Huang Y, Giorgio I, Xu F. 2023 Wrinkling of twisted thin films. *Int. J. Solids Struct.* **262**, 112075. (doi:10.1016/j.ijsolstr.2022.112075)
77. Li J, Chen Y, Feng X, Feng J, Sareh P. 2021 Computational modeling and energy absorption behavior of thin-walled tubes with the Kresling origami pattern. *J. Int. Assoc. Shell Spat. Struct.* **62**, 71–81.
78. Kwak H, Lee J, Kim J, Jo H, Ki K, Lee A. 2026 Wrinkling of thin films in pre-stretched soft substrate trilayers. *Int. J. Mech. Sci.* **312**, 111213. (doi:10.1016/j.ijmecsci.2026.111213)
79. Tan B, Lyu J, Yang F, Xu K, Qiao S, Song B, Yang L, Liu K. 2026 Bistable origami thermal switch with high switching ratios. *Nat. Commun.* **17**, 3177. (doi:10.1038/s41467-026-69956-2)
80. Jankauski M, Schwab R, Casey C, Mountcastle A. 2022 Insect wing buckling influences stress and stability during collisions. *J. Comput. Nonlinear Dyn.* **17**, 111002. (doi:10.1115/1.4055309)

81. Parle E, Herbaj S, Sheils F, Larmon H, Taylor D. 2016 Buckling failures in insect exoskeletons. *Bioinspir. Biomim.* **11**, 016003. (doi:10.1088/1748-3190/11/1/016003)
82. Bayly PV, Taber L, Kroenke CD. 2014 Mechanical forces in cerebral cortical folding: a review of measurements and models. *J. Mech. Behav. Biomed. Mater.* **29**, 568–581. (doi:10.1016/j.jmbbm.2013.02.018)
83. Garcia K, Kroenke C, Bayly P. 2018 Mechanics of cortical folding: stress, growth and stability. *Phil. Trans. R. Soc. B* **373**, 20170321. (doi:10.1098/rstb.2017.0321)
84. Mallela AN, Deng H, Gholipour A, Warfield SK, Goldschmidt E. 2023 Heterogeneous growth of the insula shapes the human brain. *Proc. Natl Acad. Sci. USA* **120**, e2220200120. (doi:10.1073/pnas.2220200120)
85. Javadi Y, Fernandez JM, Perez-Jimenez R. 2013 Protein folding under mechanical forces: a physiological view. *Physiology* **28**, 9–17. (doi:10.1152/physiol.00017.2012)
86. Forman JR, Clarke J. 2007 Mechanical unfolding of proteins: insights into biology, structure and folding. *Curr. Opin. Struct. Biol.* **17**, 58–66. (doi:10.1016/j.sbi.2007.01.006)
87. Douglas SM. 2017 Bringing proteins into the fold. *Science* **355**, 1261–1262. (doi:10.1126/science.aam9541)
88. Liu K, Paulino GH. 2018 Highly efficient nonlinear structural analysis of origami assemblages using the MERLIN2 software. *Origami* **7**, 1167–1182.
89. Sigmund O. 2001 A 99 line topology optimization code written in Matlab. *Struct. Multidiscipl. Optim.* **21**, 120–127. (doi:10.1007/s001580050176)
90. Chudoba R, van der Woerd J, Hegger J. 2014 *Numerical modeling support for form-finding and manufacturing of folded-plate structures made of cementitious composites using origami principles* (eds N Bićanić, H Mang, G Meschke, R de Borst), pp. 451–461. Leiden, The Netherlands: CRC Press.
91. Munro D. 2024 A simple QP modification of the OC update to permit treatment of the topology design problem of self-weight. *Struct. Multidiscipl. Optim.* **67**, 25. (doi:10.1007/s00158-024-03753-7)
92. Huang R. 2005 Kinetic wrinkling of an elastic film on a viscoelastic substrate. *J. Mech. Phys. Solids* **53**, 63–89. (doi:10.1016/j.jmps.2004.06.007)
93. Tang Y, Wang W, Duan H, Liu K. 2026 Concurrent topology and geometry optimization of origami structures via strain energy minimization. Figshare. (doi:10.6084/m9.figshare.c.8561980)

Glossary

Latin symbols

$\bar{C}_{dy}^{(\omega)}$	Dynamic crease-length ratio
$\boldsymbol{F}$	Nodal external force vector
F_m^S	Sensitivity of U with respect to x_m
k_H^B, k_H^F	Bending/folding hinge stiffness
k_{Hj}	Stiffness of hinge element j
L_{Cj}	Equivalent crease length
L_{Hj}	Hinge length (current configuration)
$\boldsymbol{u}$	Nodal displacement vector
U_{Bi}, U_{Hj}	Bar/hinge strain energy
$\boldsymbol{x}$	Vector of nodal coordinates
K_{ss}	Equivalent substrate stiffness
m	Move limit (topology optimization)
M	No. of optimized nodal coordinates

(*Continued*.)

N	Total number of nodes
N_1, N_2	No. of bar and hinge elements
S_i	Second P-K stress in bar element i
t_j	Topological design variable
$\boldsymbol{t}$	Vector of topological variables
U	Total structural strain energy
$\widetilde{U}$	Linearized objective function
x_m	Single nodal coordinate component
Greek symbols	
β	Stiffness interpolation coefficient
η	Scaling factor for move limit
Π	Total potential energy, $U - V$
$\xi^{\mathrm{TO}}, \xi^{\mathrm{SO}}$	Convergence tolerance (topology/geometry)
Δs	Move limit (geometry optimization)
θ_j, θ_j'	Dihedral angle (before/after)
ϕ	Stopping threshold (outer)
ω	Outer evolution step index